J. Fluid Mech. (1980), *vol.* 98, *part* 1, *pp.* 97–135
Printed in Great Britain

A 'turbulent spot' in an axisymmetric free shear layer. Part 2

By A. K. M. F. HUSSAIN, S. J. KLEIS AND M. SOKOLOV†
Department of Mechanical Engineering, University of Houston, Texas 77004

(Received 9 April 1979 and in revised form 4 September 1979)

The mechanics of a spark-induced coherent structure (called a 'spot') in the turbulent mixing layer of a 12·7 cm diameter incompressible air jet has been investigated through phase-locked measurements at three streamwise stations. Phase averages have been obtained from 200 realizations of X-wire (time-series) data after these are optimally time-aligned with respect to one another through an iterative process of maximization of cross-correlation of individual realizations with the ensemble average. Realizations that are grossly out of alignment owing to turbulence-induced distortions have been rejected; the rejection ratio increases with increasing radial position. Data include phase-average time series of background turbulence intensities, coherent and background Reynolds stresses, vorticity and intermittency at different transverse positions. Spatial distributions of these properties over the extent of the spot have been presented as contour maps. The computed pseudo-stream-functions have been compared with the phase-average streamlines inferred from the measured distributions of the velocity vector. Comparison with the phase-average intermittency contours show that the pseudo-stream-functions are reliable and, even though the integration involved produces smoothed-out stream functions, are most useful in deducing the structure dynamics and its convection velocity.

The spark-induced spot is an elongated large-scale coherent vortical structure spanning the entire thickness of the mixing layer, which moves downstream at a convection velocity of about $0{\cdot}68U_e$. The dynamics of the turbulent mixing layer spot, whose signature is buried in the large-amplitude background fluctuations, is much more complicated than that of the boundary-layer spot. The spot transports jet-core fluid outwards at its front and entrains ambient fluid primarily at its back; the outward-momentum transport dominates the inward transport. The Reynolds stress contribution by the spot structure is noticeably larger than that due to the background turbulence. The coherent structure vorticity is significantly modified by the structure-induced organization of the background Reynolds stress at the locations of 'saddle points' of the latter's distribution. The vorticity, intermittency and other turbulence measures, zone averaged over the extent of the spot, compare well with the time-average values, thus suggesting that the spark-induced 'spot' is probably not different from a naturally occurring large-scale coherent structure.

† Present address: School of Engineering, Tel-Aviv University, Israel.

0022–1120/80/4437–8650 $02.00

1. Background

The increasing awareness of the presence of the large-scale coherent structures in turbulent shear flows and their possibly dominant role in the transports of heat, mass and momentum and in the production of aerodynamic noise have been the motivation for continuing investigation of the coherent structures in the near fields of circular jets in our laboratory (Zaman 1978; Clark 1979). Even though the existence of these structures and their organized interactions (like pairing) have been conclusively demonstrated in flows that otherwise possess all the symptoms of fully-developed (random) turbulence (Brown & Roshko 1974; Winant & Browand 1974; Browand & Laufer 1975; Hussain & Zaman 1975, 1980), their occurrence has not been necessarily accepted as universal. In fact, Chandrsuda *et al.* (1978) contend that the Brown–Roshko roller-type large-scale coherent structure in a mixing layer is a legacy of the upstream instability and that these structures will be three-dimensional when the Reynolds number or the free-stream turbulence is high (see also Yule 1978; Pui & Gartshore 1978; Hussain & Zaman 1980; Hussain & Clark 1980). The evolution of the mixing-layer characteristics has been shown to be dependent on the initial-mean and turbulence characteristics (Hussain & Zedan 1978*a*, *b*) or controlled excitation (Oster *et al.* 1978; Zaman 1978), which presumably influence the coherent structure.

Clark (1979) has visually observed that the axisymmetric mixing layer is well organized at lower Reynolds numbers but is essentially disorganized at higher Reynolds numbers. Surprisingly, the ciné films produced show that the mixing layer is more organized when tripped, i.e. when the efflux boundary layer demonstrates all characteristics of the equilibrium flat-plate turbulent boundary layer, than when untripped. The pictures show that tearing (when a structure is divided into two or more parts) is at least as dominant a mode of coherent-structure interaction as pairing. Zaman's (1978) data in a jet under controlled excitation document the jet response to the excitation and the spatial distributions of the flow properties over the extent of the vortical structures at different phases of the pairing event. These data show that significant Reynolds stress production is associated with the pairing process and that, even when the initial vortex roll-up is organized through controlled excitation, the initially toroidal vortices develop three-dimensionality before breakdown near the end of the potential core, where the controlled excitation seems to have little effect in retaining circumferential coherence (Hussain & Zaman 1980; see also Yule 1978; Davies & Baxter 1978).

Since the evolution of three-dimensionality in the initially toroidal structure in an axisymmetric shear layer has no preferred azimuthal location or orientation, quantitative characterization of the evolution of the three-dimensional structure will require complex conditionally-sampled measurements involving multiple probes. Such measurements are subject to a number of constraints. The detection depends on subjectively chosen features of the coherent-structure signatures like velocity, vorticity, temperature, etc. In the case of the axisymmetric mixing layer, the educed coherent-structure characteristics and convection velocities have been found to be dependent on whether the detection is based on the positive or negative spikes in the u signal as well as on the strengths of these spikes (Lau & Fisher 1975; Bruun 1977). In addition to the randomness in their arrival times at a particular measurement location, there are large variations in the shape, size, location, orientation and strength of the structure

from one realization to another. Each realization may capture a different cut of the structure so that the straightforward average over a large ensemble would not capture the individual-structure characteristics. There is apparently a large radial variation in the organization of the structure (Yule 1978; Lau 1978, private communication). The structure interactions like pairing or tearing further complicate its detection and eduction. Also, even if care is taken to circumvent or eliminate these complicating factors, eduction of stable ensemble averages will be extremely time consuming.

In an attempt to devise an experiment which is free from the above-mentioned constraints, it was decided to trigger the creation of a three-dimensional structure at the origin of the mixing layer through the introduction of a spark, and track its evolution downstream by using the spark trigger as the time reference for phase lock. While the present experimental approach is comparable to that in the boundary layer (Wygnanski, Sokolov & Friedman 1976; Zilberman, Wygnanski & Kaplan 1977), it must be recognized that the mechanisms involved are significantly different. Since the spark-induced structure – called a 'spot' for simplicity – is quite overshadowed by the evolving large-amplitude (random) fluctuations in the mixing layer, it is a much more difficult experimental task to educe the 'spot' signature in the mixing layer than in the boundary layer. The signal alignment through iterative cross-correlation in the mixing-layer case is much more complex and, consequently, the rejection ratio would be typically much higher. The spot in the mixing layer does not possess a self-preserving shape and undergoes large distortions through turbulence-induced 'jitter' in the convection speed and its shape, size and orientation, thus further compounding the detection as well as discussion of its dynamics.

The experimental details and procedures, the data analysis and signal enhancement techniques and the phase-average streamwise velocity data were presented in part 1 (Sokolov *et al.* 1980; hereinafter referred to as I). This part discusses the detailed distributions of the phase-average coherent and background Reynolds stresses, vorticity, intermittency, streamlines and pseudo-stream-functions and attempts to discuss the dynamics of the spark-induced coherent structure.

Note that the zone-average r.m.s. intensities are essentially the same as the time-average intensities and the maximum departure of the phase-dependent intensity from the time-average intensity is no more than 20 %. Only on the low-speed side is the phase-dependent intensity comparatively more pronounced, as is expected. Thus the spot is indeed a relatively weak structure in comparison with the background turbulence (see I).

2. Phase average

The appropriate approach to characterizing the evolution of the spark-induced (spot) structure is to obtain ensemble-average measurements locked to the spark trigger at a particular phase of the structure as it travels past a detection probe. Discussion of the spot dynamics thus requires a clear understanding of the phase-averaging operation. Especially, the interpretation of the coherent and background Reynolds stresses requires derivation of the governing equations for the phase-average flow variables.

In the presence of the spot structure, the signal f of any flow variable can be assumed

to consist of an organized-structure component f_p superimposed on the background-turbulence (phase random) fluctuation f_r (Hussain 1977). Thus

$$f(\mathbf{x},t) = f_p(\mathbf{x},t) + f_r(\mathbf{x},t). \tag{2.1}$$

In order to separate the contributions due to the coherent and background turbulent flow fields, it is necessary to employ the *phase average* (Hussain & Reynolds 1970). The phase average $\langle f \rangle$ of f at any phase ϕ at $\mathbf{x}$ is defined as

$$\langle f(\mathbf{x},\phi)\rangle = \lim_{N\to\infty} \frac{1}{N} \sum_{n=1}^{N} f(\mathbf{x},\phi+n\omega\tau), \tag{2.2}$$

where ω is the circular frequency of the periodic occurrence of the structure and τ the period. If t is the time within a period corresponding to ϕ, then

$$\langle f(\mathbf{x},t)\rangle = \lim_{N\to\infty} \frac{1}{N} \sum_{n=1}^{N} f(\mathbf{x},t+n\tau), \tag{2.3}$$

that is,

$$f_p(\mathbf{x},T) \equiv \langle f(\mathbf{x},t)\rangle, \quad 0 \leqslant T \leqslant \tau.$$

In a practical experiment, the phase average need be taken over only a finite ensemble size N. The adequacy of the ensemble size N is determined from the convergence of the phase-average data. For the present case, suppose the spark is triggered at intervals τ apart. In order to capture the spot signature, the data at any x station will be sampled at intervals τ apart. If data at a particular phase ϕ with respect to the spark trigger are desired, then the signal will be sampled at that ϕ over a large number of realizations. The average of the data is the phase average at that ϕ since background turbulence being random will cancel out over a large number of cycles. If this average is repeated over a range in ϕ covering the spot signature, we will obtain the required phase-average distribution in time at the measurement location. Thus, given an instantaneous signal and the period between successive sparks, the coherent and random parts of the signal can be separated.

Since the spark-generation period can be chosen at will, it is desirable to space the formation of the spot such that two successive spot structures do not interact with each other; thus, the educed phase-average coherent structure is that of a single spot in the mixing layer. This requires that the period between successive sparks must be much larger than the structure passage time at any measurement station. In the present case, data spanning the spot signature occupy only a fraction (about 4 %) of the interval between sparks. It must be recognized that, in the current experiment, the background turbulence will probably include naturally occurring coherent structures also, but these would occur randomly and leave no lasting footprints (except the conventional time-mean values) in the phase average. Consequences of the phase-averaging scheme are

$$\langle f_r \rangle = 0; \quad \langle f_p f_r \rangle = 0. \tag{2.4}$$

The second relation in (2.4) states that the coherent and random components are uncorrelated. It should be emphasized that this relation should not be taken to suggest that the coherent and random components are unrelated. On the contrary, noticeable turbulence production may be associated with the spot and can be confirmed by non-zero phase-average contributions like $\langle f_r g_r \rangle$ or phase-dependent intensity f_r' (see later). The question then naturally arises as to how much of the $\langle f_p \rangle$ and $\langle f_p g_p \rangle$ data, attri-

buted to the coherent structure, is really due to periodic modulation of the background field. This concern can be relieved by realizing that the characteristic time scale of the spot coherent motion is much larger than that of the background turbulence field. Thus, even if the background turbulence intensity around the spot may be higher, when phase averaged over a large number of realizations, superposition of these random small-scale turbulent eddies will cancel out. That is, even when $f_r(t)$ is affected by the spot, $\langle f_r' \rangle$ contributes nothing to $f_p(t)$.

Substituting the decomposition (2.1) into the incompressible continuity and momentum equations, one gets, for the phase-average flow field,

$$\partial \langle u_i \rangle / \partial x_i = 0, \tag{2.5a}$$

and

$$\frac{\hat{D}}{Dt}\langle u_i \rangle = -\frac{1}{\rho}\frac{\partial \langle p \rangle}{\partial x_i} + \frac{\partial}{\partial x_j}\left(\nu \frac{\partial \langle u_i \rangle}{\partial x_j} - \langle u_{ri} u_{rj} \rangle\right), \tag{2.5b}$$

where

$$\frac{\hat{D}}{Dt} = \frac{\partial}{\partial t} + \langle u_j \rangle \frac{\partial}{\partial x_j} \tag{2.5c}$$

is the time derivative associated with a fluid particle moving in the phase-average flow field (note, there is no summation over the subscript r). The corresponding background turbulent-momentum equation is

$$\frac{\hat{D}}{Dt} u_{ri} = -\frac{1}{\rho}\frac{\partial p_r}{\partial x_i} - \frac{\partial}{\partial x_j}(\langle u_i \rangle u_{rj}) + \frac{\partial}{\partial x_j}\left[\nu \frac{\partial u_{ri}}{\partial x_j} - (u_{ri} u_{rj} - \langle u_{ri} u_{rj} \rangle)\right]. \tag{1.6}$$

The second term on the right-hand side represents organized-field momentum transport by the background turbulence. $-\rho \langle u_{ri} u_{rj} \rangle$ represents the contribution of the background turbulent field to the phase-average field and is termed the phase-average Reynolds stress. It is the stress responsible for extraction of the phase-random turbulent kinetic energy from the phase-coherent field through the work of $-\rho \langle u_{ri} u_{rj} \rangle$ against the structure-induced shear rate $\partial \langle u_i \rangle / \partial x_j$.

For energy equations of the phase-average and background turbulent fields and discussions of the energy exchanges between these two fields, and the associated flow physics, see Hussain (1977).

For convenience, we will denote the coherent component of $f(\mathbf{x}, t)$ by f_p, its random component by f_r. Thus, $u = u_p + u_r$ and $v = v_p + v_r$, and $\langle u_r v_r \rangle$ is the phase average of the background-turbulence Reynolds stress. We will also denote u_r', v_r' as the *phase-average r.m.s.* values defined as

$$f_r' = \left[\lim_{N \to \infty} \frac{1}{N} \sum_{n=1}^{N} f_r^2(x, \phi + 2\pi n)\right]^{\frac{1}{2}}. \tag{2.7}$$

Note that if the phase-average field is further decomposed into a time-independent field and a time-dependent field (Hussain & Reynolds 1970), i.e.

$$f(\mathbf{x}, t) = \bar{f}(\mathbf{x}) + \tilde{f}_p(\mathbf{x}, t) + f_r(\mathbf{x}, t), \tag{2.8}$$

then $-\rho \tilde{u}_i \tilde{u}_j$ will denote the coherent-field Reynolds stress. This decomposition is meaningful when the organized field can be regarded as a perturbation of the mean field, but is not very useful in the present situation where the coherent structure is not a superimposed structure on the time-mean field. At the location of the structure, the flow is essentially due to the structure. Furthermore, the mean-field is presumably mainly due to the superposition of many such coherent structures.

3. Procedure

This study was carried out in the near-field of a 12·7 cm diameter circular air jet operated at the exit speed of 20 m s^{-1}. See I for details of the apparatus. Hot-wire data were obtained at different radial positions in the mixing layer at the three x stations corresponding to $x/D = 1{\cdot}5$, 3·0 and 4·5. The radial position at each station is characterized by the co-ordinate $\eta = (y - \frac{1}{2}D)/x$. For correspondence between the η values and the U/U_e values as well as for documentation of the basic flow state, see I. Time-series data from a linearized X-wire were recorded on-line, the A/D converter being triggered such that 500 data points, sampled at 8·4 kHz, spanned the coherent structure signature. The time delay for the trigger was determined from the streamwise distance of the station from the spark location and the approximate convection velocity of the structure. Ensemble averages were obtained from 200 realizations after the time-series data were aligned with respect to one another through an iterative method of maximization of cross-correlations of individual realizations with the ensemble average. Since the spot was expected to be a large-scale entity, each signal was low-pass filtered at 500 Hz in order to hasten the iteration process. Further signal enhancement was achieved through rejection of the realizations requiring excessive time shifts.

In addition to the $u(t)$ and $v(t)$ data, intermittency $I(t)$ data were taken on-line. The motivation for obtaining intermittency data was to use an independent criterion for detection of the spot signature. Since the spot is embedded in the turbulent mixing layer, the intermittency detector will detect both the spot and the turbulent mixing layer. However, the naturally occurring structures in the mixing layer as well as the boundaries of the layer being random, the phase-average contribution locked to the spot will highlight only the region occupied by the spot. Since the intermittency detection is based primarily on the high-frequency content of the $v(t)$ signal, it gives an independent method of spot detection compared to that based on the phase average u_p, v_p, or ζ_p data which are biased towards the low-frequency, large-amplitude components of the spot signature.

Measurement of intermittency has been carried out by numerous investigators and the criteria used vary widely. Since random vorticity is the only characteristic identifier of a turbulent region, all intermittency detection criteria must somehow relate to vorticity fluctuations. Typically, the z component of vorticity $\zeta = \partial v/\partial x - \partial u/\partial y$ is used for detection. However, since ζ alone requires a multi-wire probe, it was decided to use only $\partial v/\partial x$ for turbulence detection. In order to further simplify detection, it was decided to use a single X-wire probe and apply the Taylor hypothesis, i.e. assume $\partial v/\partial x = -(1/U)\,\partial v/\partial t$. Thus, high-frequency fluctuations in $\partial v/\partial t$ may be taken as an indicator of vorticity fluctuations. While both turbulent and non-turbulent portions across an interface can have velocity fluctuations of comparable amplitudes, the fluctuations in the turbulent region contain small scales and thus higher frequencies. This characteristic can be taken advantage of by including the second time-derivative $\partial^2 v/\partial t^2$ in the intermittency detection. Detection based on the rectified derivatives of the velocity signal has been used by many investigators.

Figure 1 shows the schematic of the detection circuit; the two inputs E_1 and E_2 are the linearized outputs from the two wires of the x-wire probe. The circuit as well as the criteria for detection are essentially the same as those used by Kleis (1974). Note that the intermittency detection is based on the signal

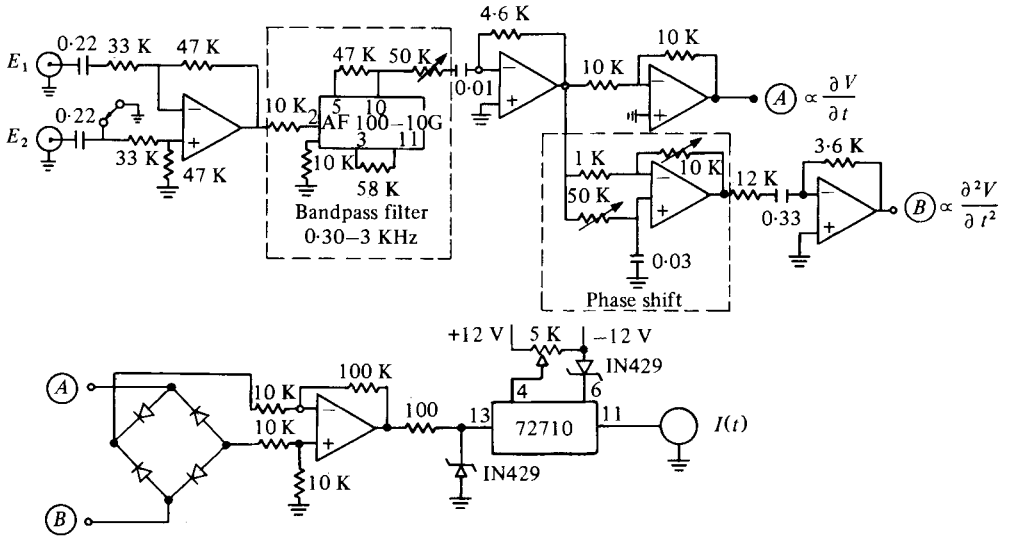

FIGURE 1. Schematic diagram of the intermittency detection circuit.

$$e(t) = |\partial v/\partial t| + A\,|\partial^2 v/\partial t^2|. \tag{3.1}$$

The $v(t)$ signal is bandpass filtered in the range 300 Hz to 3 kHz in order to emphasize the high-frequency velocity oscillations but exclude noise. Note that the phase shifts in the $\partial^2 v/\partial t^2$ signal would be such as to smooth out the oscillations due to $|\partial v/\partial t|$ in $e(t)$ and thus facilitate better detection through reduction of 'drop-outs', which are normally eliminated through smoothing of $I(t)$. The ratio A between the second and first derivatives in (3.1) was chosen such that the r.m.s. amplitudes of the two terms were approximately equal. Spot checks of the time-average intermittency γ as a function of the detection threshold e_{th} showed that γ is insensitive over a good range in e_{th}. The threshold level chosen was within this range.

Since $u(t)$, $v(t)$ and $I(t)$ signals are all derived from the same X-wire probe in the flow, they all should capture the same flow features simultaneously. Thus, the time shifts in the $v(t)$ and $I(t)$ arrays for optimum alignment were assumed to be the same as those for the corresponding $u(t)$; consequently, the $v(t)$ and $I(t)$ realizations corresponding to the rejected $u(t)$ realizations were also rejected. Also, the radial variations of the time-shift histograms and rejection ratios for $v(t)$ and $I(t)$ at the three measurement stations are the same as for $u(t)$.

As explained in I, enhancement of the coherent-structure signature was achieved through rejection of 'bad' realizations before obtaining ensemble averages. The rejection was determined on the basis of excessive time shifts required for optimum alignment and was justified on the grounds that bad realizations represent spots which have been subjected to excessive distortions and thus should be excluded from the ensemble averages. Thus, the probability-density functions of the time shifts, as well as the radial profiles of the rejection ratios, are themselves interesting features of the mixing layer physics. Realizations requiring time shifts more than 3 standard deviations of all time shifts at each location were rejected. The rejection ratio, i.e. fraction of realizations rejected on the basis of the above-mentioned criteria, increased rapidly

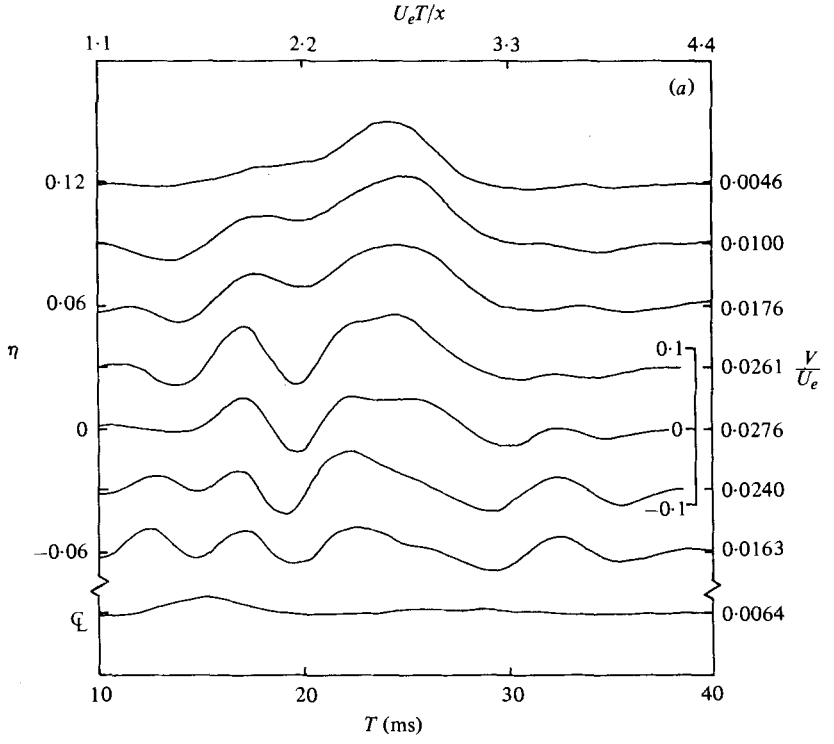

FIGURE 2 (*a*). For legend see page 105.

from nearly zero on the core side to larger values (viz. 15 % at station 1, 45 % at station 2 and 51 % at station 3) on the outer edge of the mixing layer. The standard deviation σ of the time shifts increases rapidly across the mixing layer towards the outer edge except at station 1, where the radial variation of σ is smaller (see I). Since time shifts are measures of distortion of the spot by the naturally occurring background turbulence, these large radial variations of σ and rejection ratio would appear to be a result of interactions with the natural structures, which have been observed by Hussain & Clark (1980) to undergo tearing and fractional pairing starting at about $x/D \simeq 1{\cdot}0$.

4. Results

4.1. *Phase-average velocity field*

Figure 2(*a*) shows the composite of the final iteration ensemble-average transverse-velocity signals $\tilde{v}_p/U_e$ at the first station ($x/D = 1{\cdot}5$) as a function of the time delay T (ms) with respect to the spark trigger. (Note that in figures 2–12, increasing time corresponds to decreasing x and vice versa. The co-ordinates at the top of each of the figures 2–12 denote non-dimensional times U_eT/x.) For simplicity, and following Bruun (1977) and Yule (1978), we use $\eta \equiv (y - \frac{1}{2}D)/x$ as the non-dimensional transverse co-ordinate; since the virtual origin is located at $0{\cdot}13D$ upstream from the lip, it is permissible to ignore the virtual-origin effect in this respect. The $\tilde{v}_p$ traces are staggered in η marked on the left boundary of the figure; the top trace is for the largest radial

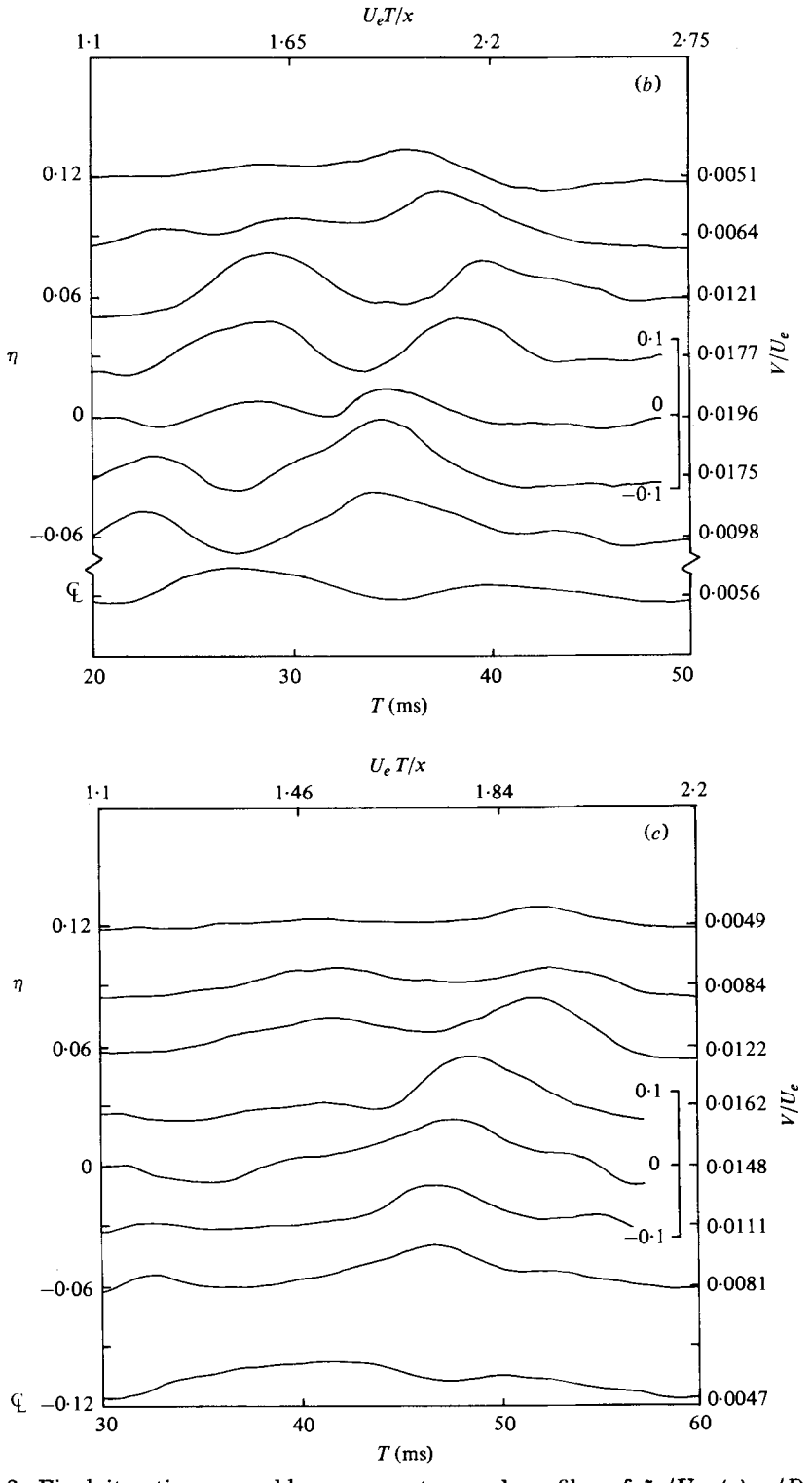

FIGURE 2. Final iteration ensemble-average staggered profiles of $\tilde{v}_p/U_e$. (*a*) $x/D = 1{\cdot}5$; (*b*) $x/D = 3{\cdot}0$; (*c*) $x/D = 4{\cdot}5$. The time-mean value V/U_e corresponding to each η is indicated on the right boundary.

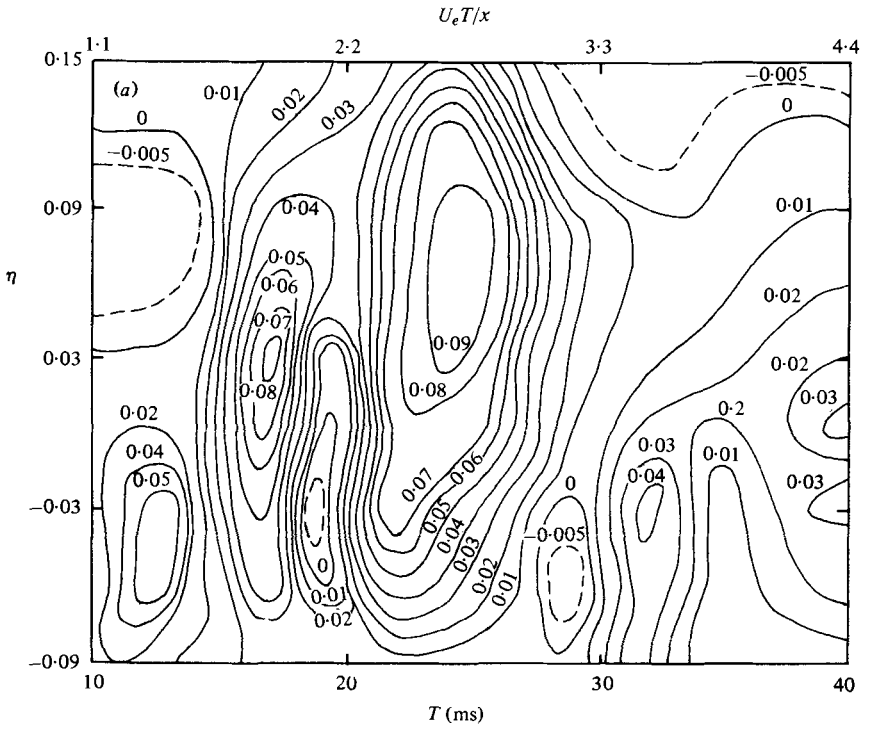

FIGURE 3(*a*). For legend see page 107.

position and the bottom one for the jet centreline; the $\tilde{v}_p/U_e$ scale is shown as an insert on the right-hand side. These time traces show phase-average deviations from the local time-mean velocity. The time-mean value V corresponding to each η is marked on the right-hand side. Figures 2(*b*) and 2(*c*) show the corresponding staggered $\tilde{v}_p/U_e$ profiles at stations 2 ($x/D = 3{\cdot}0$) and 3 ($x/D = 4{\cdot}5$). While the instantaneous time traces $v(t)$ do not show clear evidence of the underlying structure, the application of the method of optimum alignment through maximization of cross-correlation and phase averaging brings out the signature of the underlying spark-induced structure (see I). Like the $\tilde{u}_p$ data, $\tilde{v}_p(T)$ distributions also indicate a structure spanning the width of the mixing layer located, for example, at $T \approx 24$ ms in figure 2(*a*). The $\tilde{v}_p$ data show that the spot structure at station 2 is quite complex. Note that, compared to the $\tilde{u}_p$ signal, the $\tilde{v}_p$ signal on the jet centre-line is comparatively much smaller and is thus indicative of essential axisymmetry of the phase-average coherent structure induced by the spark.

In order to study the spot evolution, it is helpful to locate its centre as well as determine its boundary. For this purpose, it is convenient to use contour plots of phase-averaged properties associated with the spot. Figures 3(*a*), (*b*) and (*c*) show contours of constant values of (the total) v_p; the negative values are denoted by the dashed lines. At station 1, the radial position and the axial location (i.e. time delay T) of the maximum value of v_p, i.e. $\eta \approx 0{\cdot}06$ and $T \approx 24$ ms, agree well with the maximum of u_p (see figure 17(*a*) in I). This agreement is consistent with a high-speed parcel of fluid moving outward and thus represents transport of a significant amount of momentum normal to the shear layer (see discussion of $u_p v_p$ data later). Note that the small

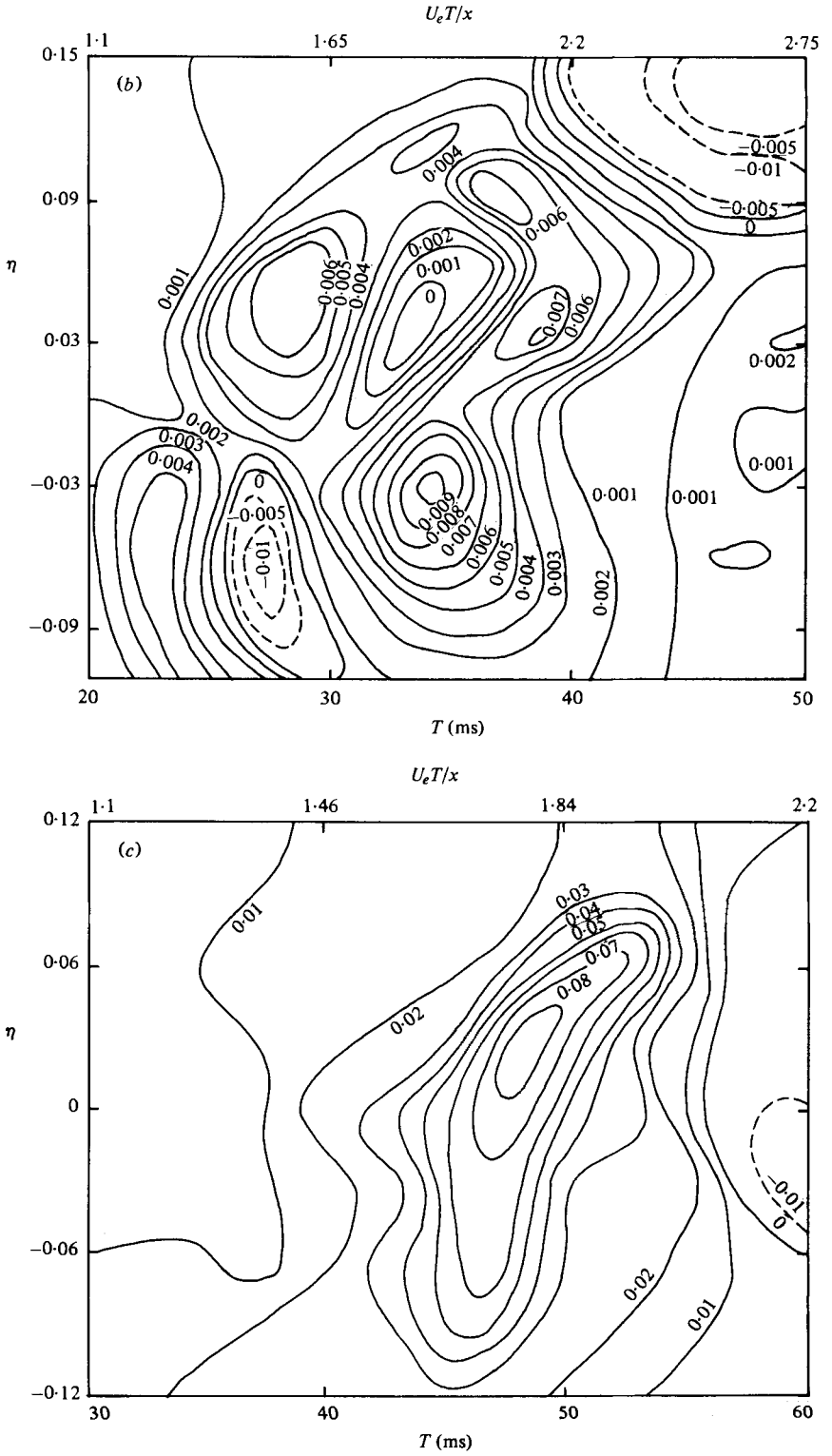

FIGURE 3. Contours of v_p/U_e. (*a*) $x/D = 1{\cdot}5$; (*b*) $x/D = 3{\cdot}0$; (*c*) $x/D = 4{\cdot}5$.

negative v_p region in figure 3(*a*) (at $\eta \simeq -0{\cdot}03$, $T \simeq 19$ ms) is embedded in the centre of a larger, negative u_p region (figure 17(*a*) in I) and should also contribute to the phase-average momentum transport $u_p v_p$ (see later). However, the radial momentum transport inward is much lower than that outward. The region of the positive peak at $T \simeq 13$ ms, $\eta \simeq 0{\cdot}03$ does not show a corresponding peak in the u_p data, thus suggesting that this part of the structure is not significant in radial momentum transport. The change in the v_p contours between stations 1 and 2 show large distortions and suggest that the high-speed part is being convected past the low-speed, outer part in a somewhat 'sliding' fashion. Recent flow visualization movies (Clark 1979) of a high-speed axisymmetric mixing layer show that even the naturally occurring structures are occasionally torn apart, i.e. sheared into two or more parts, the parts on the high-speed side moving past the structures on the low-speed side.

Even though v_p contours are not necessarily markers of the spot fluid, comparison of the structure contours in figures 2(*a*) and (*b*) suggests a clockwise rotation of the structure (in the (η, T) plane) concurrent with the sliding motion. Similar rotation, consistent with the shear-layer strain rate, is also apparent in figures 17(*a*) and (*b*) of I. The structure is significantly weakened, presumably by both breakdown and decay, by the time it reaches station 3. At this station, the peak value of v_p is located at $\eta \simeq 0{\cdot}03$ and $\tau \simeq 48$ ms. The u_p contour at this station also shows a peak at the same location, suggesting a strong radial momentum transport outward even at this downstream station. Note that there is no peak in v_p corresponding to the positive and negative peaks in u_p at $T = 34$ ms and 43 ms (figure 17*c* of I), suggesting that fluid in this region does not transport significant momentum. The u_p and v_p contours together suggest that the structure is located at $\tau \approx 24$ ms, 37 ms and 50 ms at stations 1, 2 and 3, respectively.

The staggered distributions of the phase-average r.m.s. intensity v_r'/U_e for the stations 1, 2 and 3 are shown in figures 4(*a*), (*b*) and (*c*), respectively. The corresponding radial locations η are marked on the left boundary of the figure. These figures give the deviations of v_r' over its zone-average r.m.s. value $\hat{v}_r'$, the average having been obtained through integration of v_r' over the record length, i.e. the data represent $(v_r' - \hat{v}_r')/U_e$. The $\hat{v}_r'$ value corresponding to each η is noted on the right-hand boundary. The fluctuations are the largest at station 1 and the smallest at station 3. It should be recognized that v_r' data may be taken with some reservation because of the artifacts inherent in the phase-average measurements. Even if the spots are optimally aligned, owing to the jitter in the shape, size and orientation, the phase-averaging process can contribute to v_r' mainly in the regions of large gradients. Comparison of figures 3 and 4 show that the large values of v_r' are associated with the locations of the structure centres identifiable from the v_p contours. Phase-locked measurements in the mixing layer of a circular jet under excitation also showed peak u_r' and v_r' to occur at structure centres (Zaman 1978). Since $v_p(T)$ undergoes reversal across the vortex centre, it is not obvious if v_r' is contributed mainly by jitter. However, discussion of $\langle u_r v_r \rangle$ data (see later) show that the contribution of jitter is small. Thus, one can reject phase jitter being a major contributor to v_r'.

4.2. *Coherent and background Reynolds stresses*

The phase-average contours of the spot-induced coherent Reynolds stress $u_p v_p(T)$ are shown in figures 5(*a*), (*b*) and (*c*) for $x/D = 1{\cdot}5$, $3{\cdot}0$ and $4{\cdot}5$, respectively; positive values

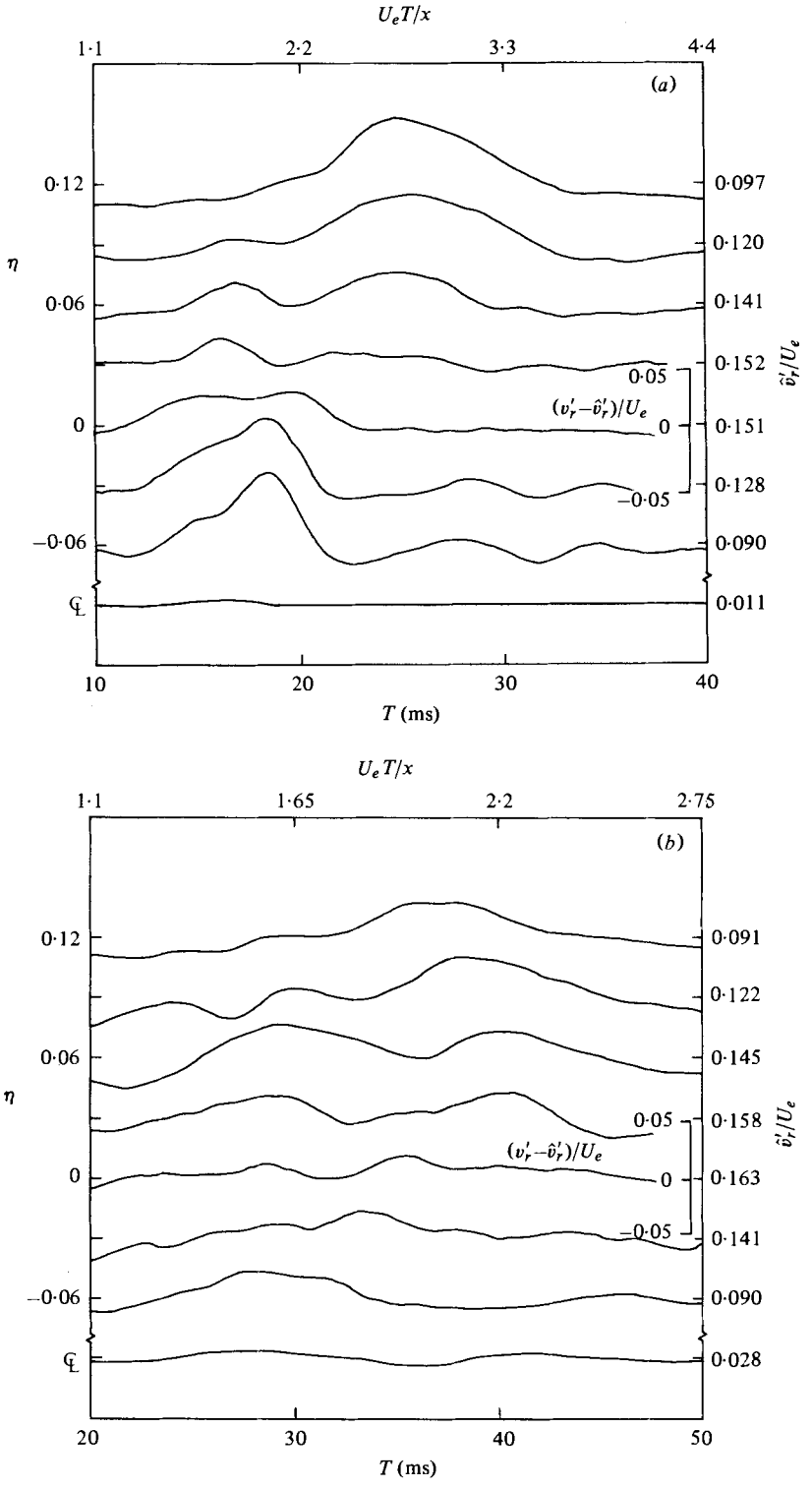

FIGURE 4 (*a*, *b*). For legend see page 110.

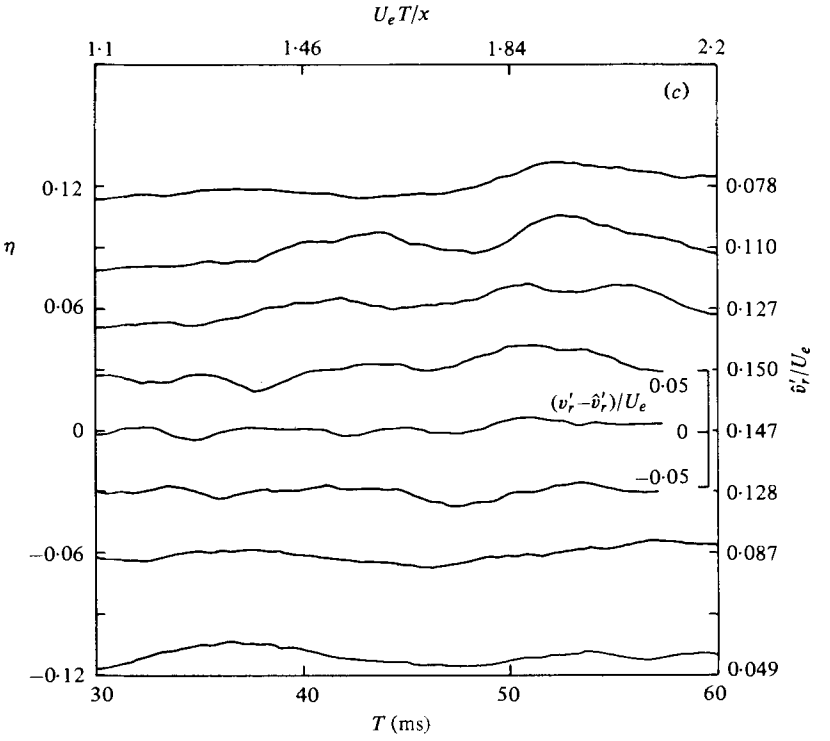

FIGURE 4. Staggered profiles of phase-average transverse intensity v'_r/U_e. (*a*) $x/D = 1{\cdot}5$; (*b*) $x/D = 3{\cdot}0$; (*c*) $x/D = 4{\cdot}5$. Zone averages $\hat{v}'_r/U_e$ over the record length corresponding to each η is indicated on the right-hand axis.

are shown by solid and negative by dotted lines. Note the amazing similarity between the v_p and $u_p v_p$ contours; even the centres of the cells agree. This shows the dominant influence of the transverse motions v_p on coherent momentum transport $u_p v_p$, as to be expected and as independently emphasized by Zaman (1978). This is exemplified at station 3, where u_p and v_p contours are different but $u_p v_p$ contours are similar to those of v_p. The $u_p v_p$ contours show that the momentum transport by the coherent structure is mostly outward; the inward momentum transport is comparatively small. If the coherent momentum transport itself is regarded as a characteristic of the spot, comparison of the $u_p v_p$ contours at stations 1 and 2 suggest some 'sliding' of the high-speed part of the spot over the low-speed part, as suggested by the v_p data. Note that between stations 2 and 3 the spot structure and transport ($u_p v_p$) become simpler as depicted by their contours while the spot's role in outward momentum transport is as dominant as in station 1.

If viewed from the time-mean velocity field, the coherent structure Reynolds stress is $\tilde{u}_p \tilde{v}_p$ (see equation (2.8)). Note, however, that this is not the total momentum transport, since $U\tilde{v}_p$ and $\tilde{u}_p V$ also represent coherent structure momentum transport. Figures 6(*a*), (*b*) and (*c*) show the contours of constant values of $\tilde{u}_p \tilde{v}_p$ for stations 1, 2 and 3, respectively. Note that the contours in figures 6(*a*), (*b*) and (*c*) are simpler than those in figures 5(*a*), (*b*) and (*c*). At each station, the contours consist of a positive and a negative transport region. Nevertheless, we believe the contours in figures 5(*a*), (*b*) and (*c*) are more meaningful in depicting the momentum transport by the spot.

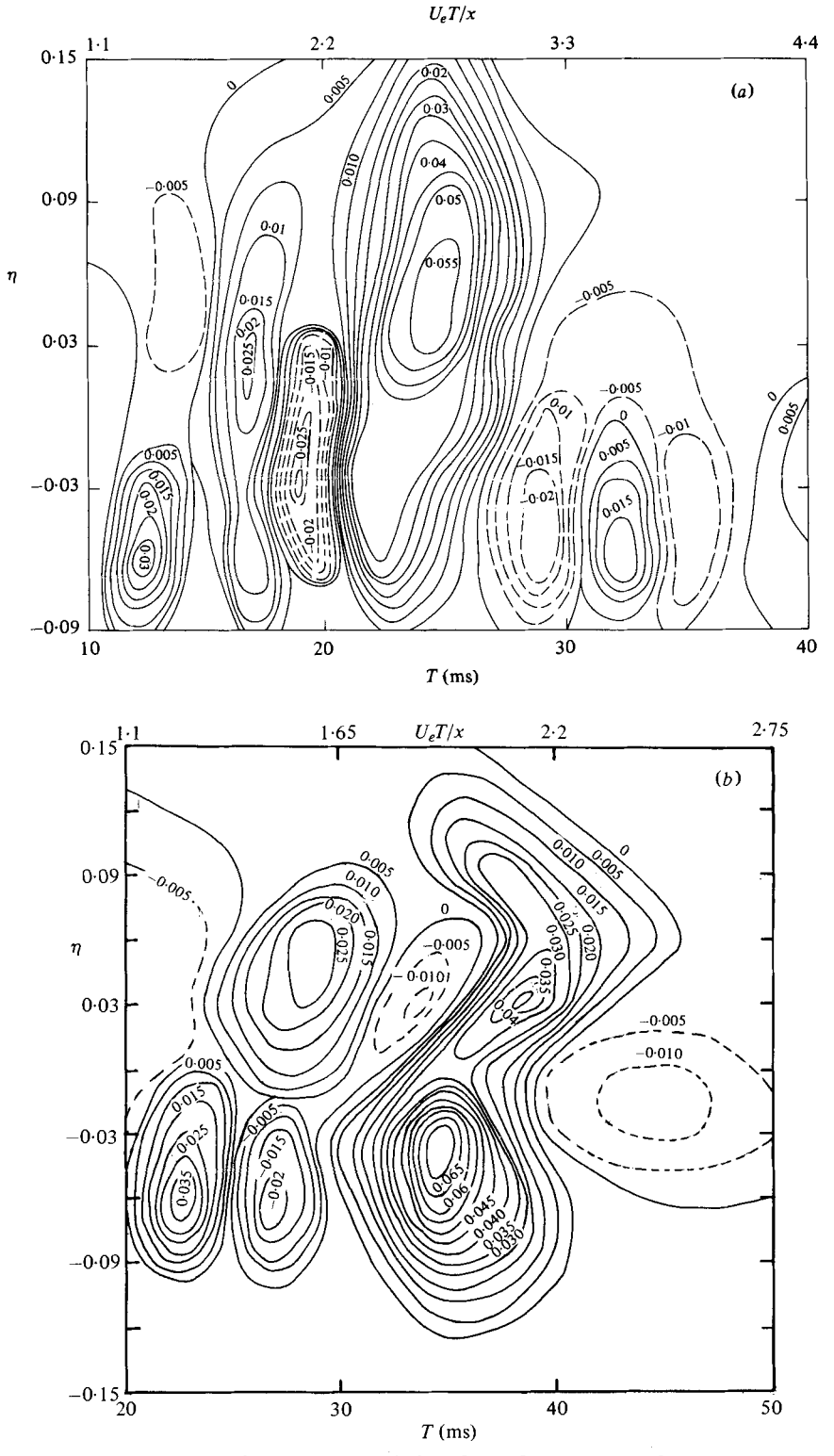

FIGURE 5 (*a*, *b*). For legend see page 112.

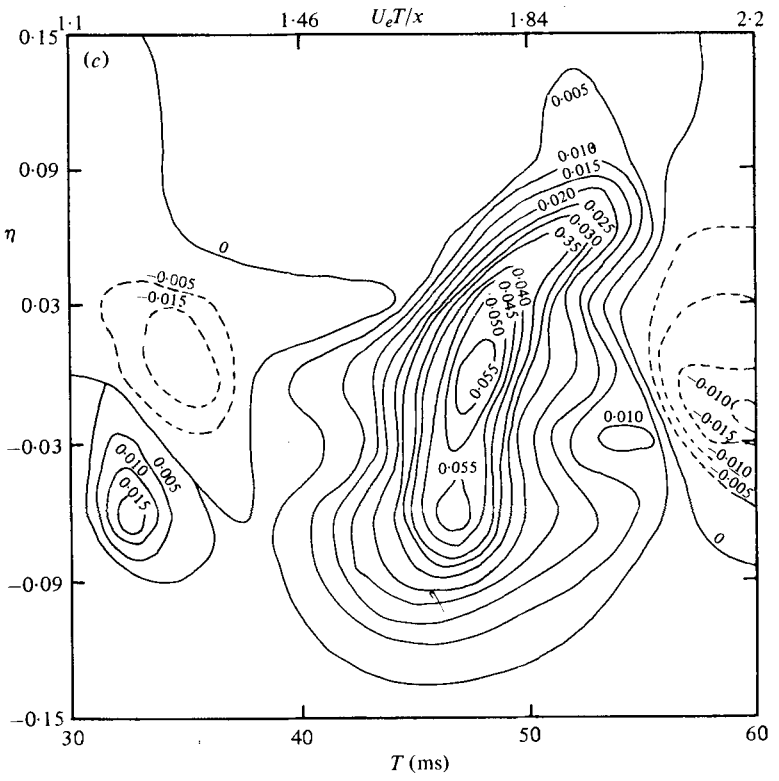

FIGURE 5. Contours of coherent structure Reynolds stress $u_p v_p / U_e^2$. (*a*) $x/D = 1{\cdot}5$; (*b*) $x/D = 3{\cdot}0$; (*c*) $x/D = 4{\cdot}5$.

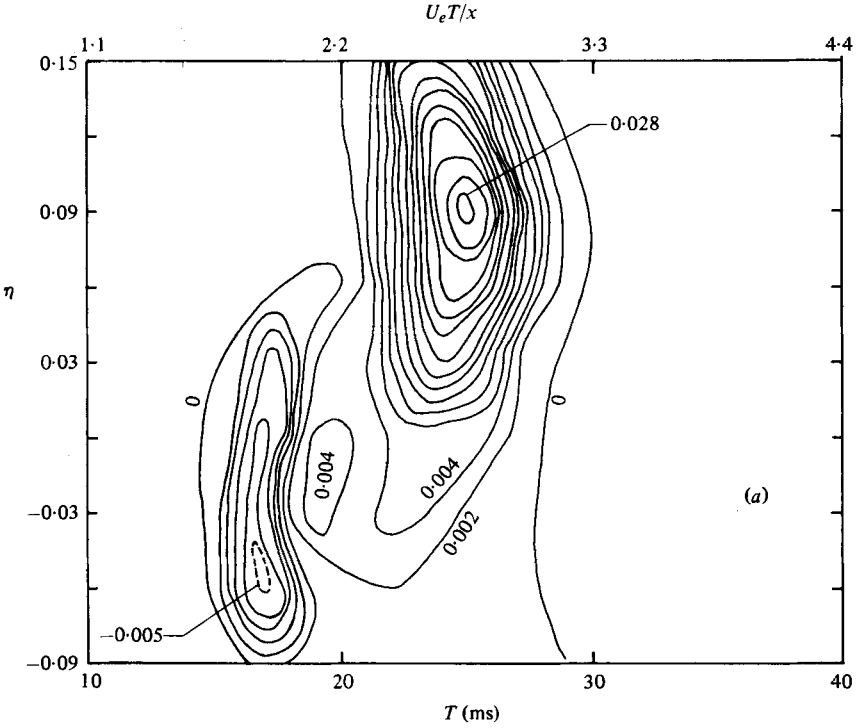

FIGURE 6 (*a*). For legend see page 113.

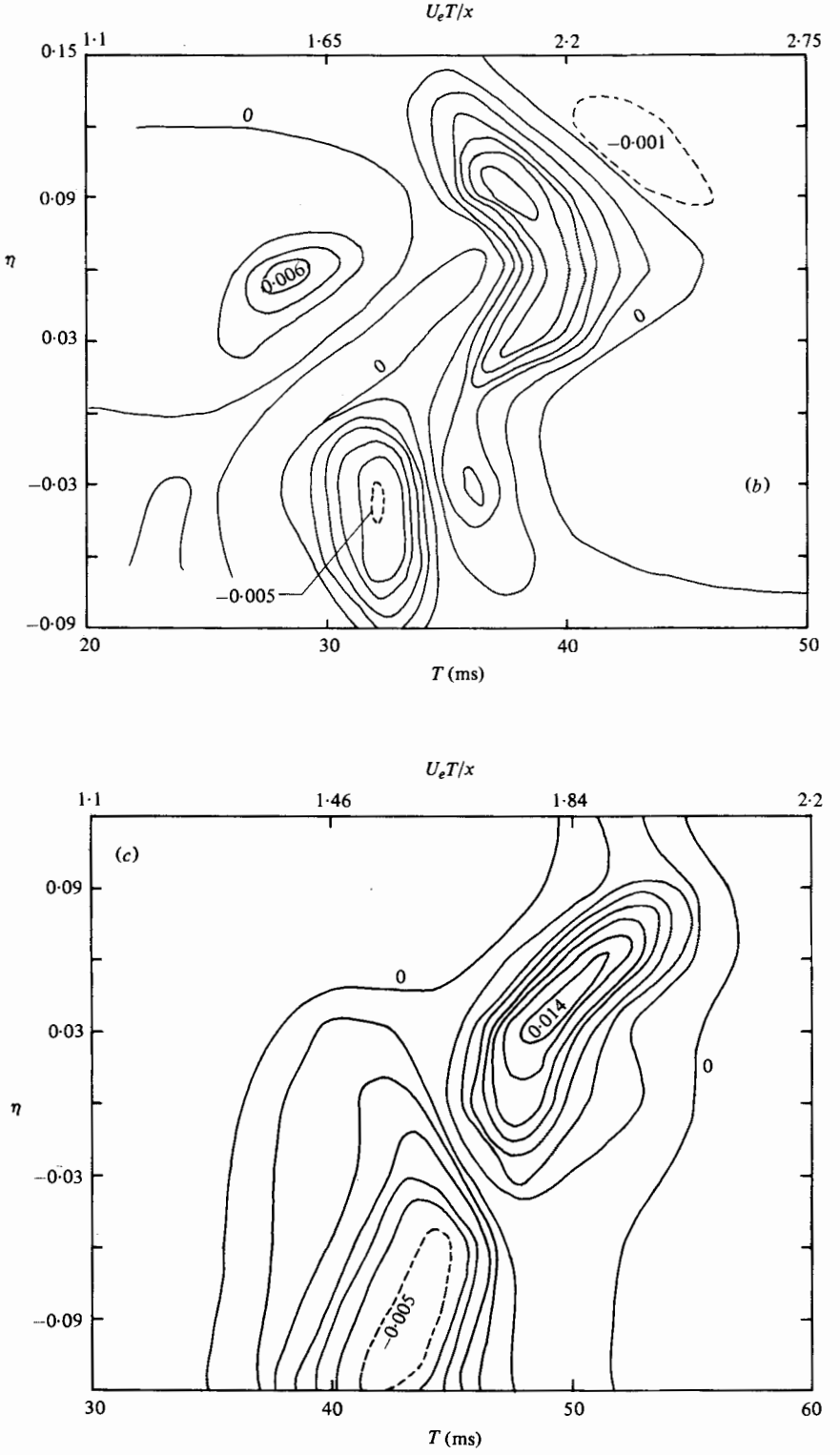

FIGURE 6. Contours of $\tilde{u}_p\tilde{v}_p/U_e^2$. (*a*) $x/D = 1{\cdot}5$; (*b*) $x/D = 3{\cdot}0$; (*c*) $x/D = 4{\cdot}5$.

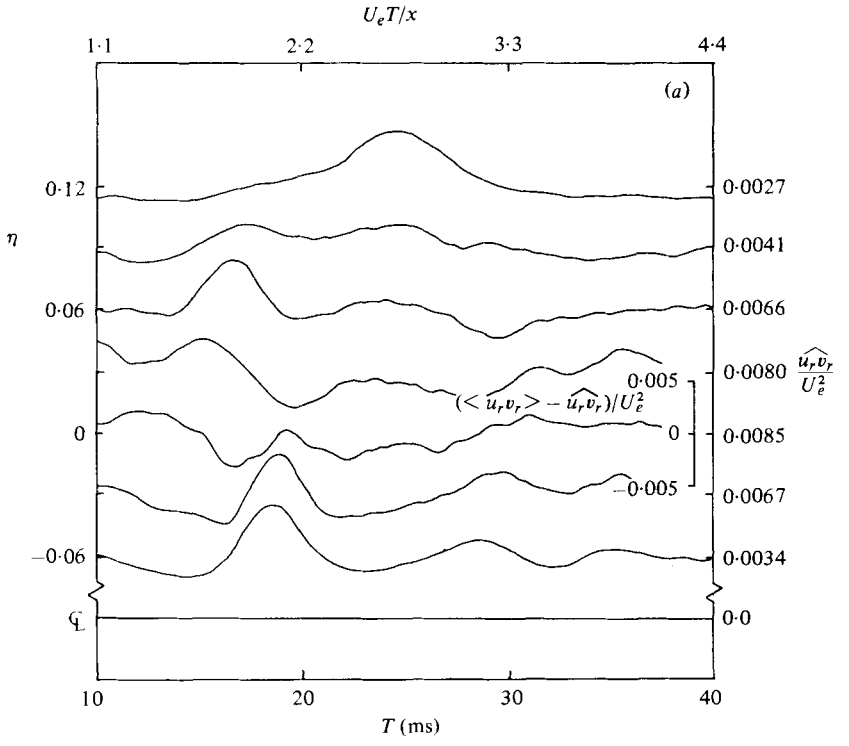

FIGURE 7 (*a*). For legend see page 115.

The phase-average traces of the background Reynolds stress $\langle u_r v_r \rangle$ are shown in figures 7(*a*), (*b*) and (*c*) for stations 1, 2 and 3, respectively. These are denoted as deviations from the zone average $\widehat{u_r v_r}$ determined by integrating $\langle u_r v_r \rangle$ over the record length; the $\widehat{u_r v_r}$ values are indicated on the right-hand boundary. At station 1, $\langle u_r v_r \rangle$ is the largest at $T \approx 25$ ms on the outer edge but at $T \approx 19$ ms on the inner edge. These two correspond to the locations of peak positive $u_p v_p$ and peak negative $u_p v_p$ values. Note that these peaks are not attributable to jitter since the $\langle u_r v_r \rangle$ peaks coincide with the centres of corresponding $u_p v_p$ contours rather than the regions of steep gradients of the latter. The $\langle u_r v_r \rangle$ data at stations 2 and 3 show no clear influence of the presence of the spot. Note also that $\langle u_r v_r \rangle$ is essentially zero on the jet centre-line at all the three stations, as to be expected. Comparison of the peak values of $u_p v_p$ and $\langle u_r v_r \rangle$ show that the former is much larger than the latter, thus suggesting that the coherent structure plays a dominant role in momentum transfer. This dominance has not decreased at station 3 where the ratio of peak $u_p v_p$ and $\langle u_r v_r \rangle$ values is around 3.

4.3. *Vorticity contours*

Figures 8(*a*), (*b*) and (*c*) show the contours of the phase-average vorticity associated with the spot. The phase-average $u_p(T)$ and $v_p(T)$ data traces were low-pass filtered in order to eliminate artificially large gradients due to the influence of the phase-random

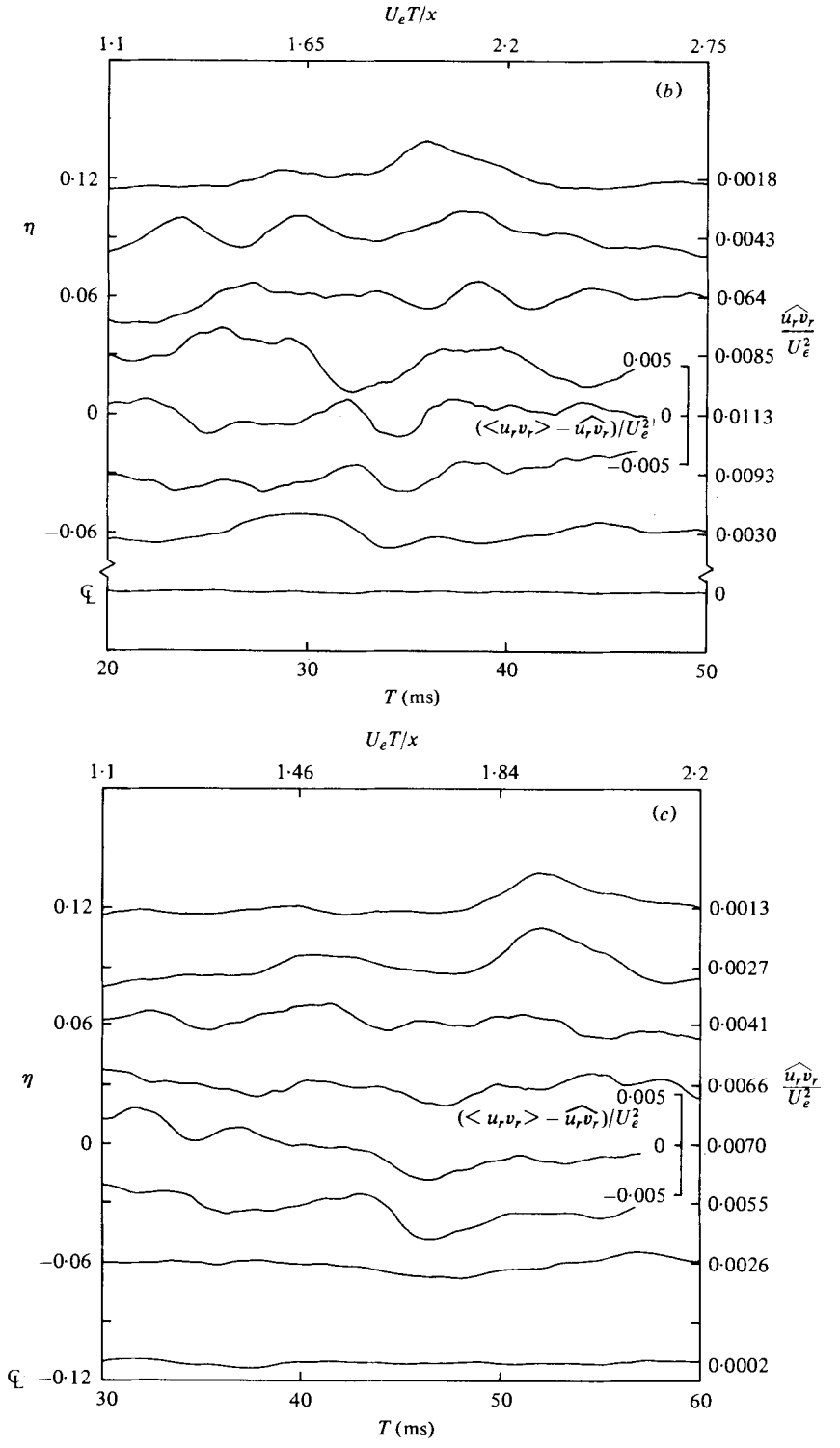

FIGURE 7. Staggered profiles of background Reynolds stress $\langle u_rv_r\rangle/U_e^2$. (*a*) $x/D = 1{\cdot}5$; (*b*) $x/D = 3{\cdot}0$; (*c*) $x/D = 4{\cdot}5$. Zone average u_rv_r/U_e^2 of $\langle u_rv_r\rangle/U_e^2$ over the record length corresponding to each η is indicated on the right-hand axis.

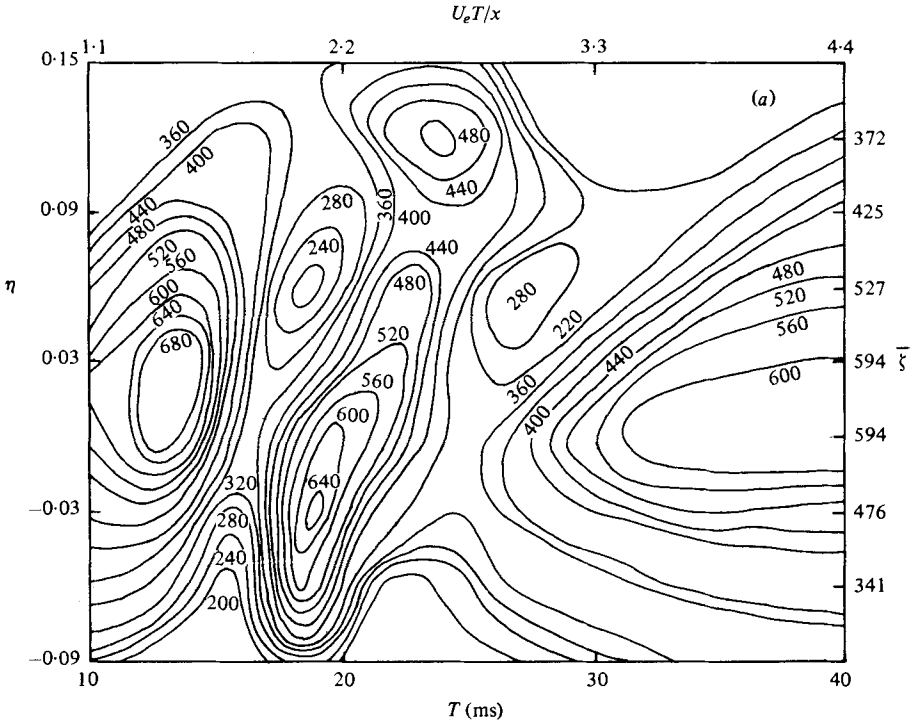

FIGURE 8 (*a*). For legend see page 117.

components on the limited-sized ensemble. The plotted vorticity ζ_p represents the z component of the phase-average vorticity $\nabla \times \mathbf{v}_p$ in the (x, r) plane, i.e.

$$\zeta_p(x,r,t) = \frac{\partial v_p}{\partial x}(x,r,t) - \frac{\partial u_p}{\partial r}(x,r,t). \tag{4.1}$$

The streamwise gradient $\partial v_p/\partial x$ was obtained by the application of the Taylor hypothesis in the frame of convection of the structure, i.e.

$$\frac{\partial v_p}{\partial x}(x,r,t) = -\frac{1}{U_c}\frac{\partial v_p}{\partial t}(x,r,t). \tag{4.2}$$

The radial gradient $\partial u_p/\partial r$ was obtained by first fitting the radial distribution of the phase-average $u_p(r)$ data at the phase under consideration with a parabola. This was done such that the point under consideration was at the middle of the three radial points through which the parabola passed. The slope of the parabola at the middle point gave the desired $\partial u_p/\partial r$.

U_c in equation (4.2) is the convection velocity of the spot. The question naturally arises as to how the convection velocity should be determined. U_c can be determined from centroids of phase-average contours of the structure-induced longitudinal or lateral velocity undulations u_p or v_p, the coherent Reynolds stresses $u_p v_p$ or $\tilde{u}_p \tilde{v}_p$, vorticity ζ_p, streamlines ψ_p, pseudo-stream-function $\langle\psi\rangle$, or intermittency γ_p. Of these, the most attractive appeared to be $u_p v_p$, ζ_p, or $\langle\psi\rangle$. The stream-function contours (discussed later), being not invariant under Galilean transformation, will be dependent on the convection velocity of the reference frame used. The use of $u_p v_p$ has

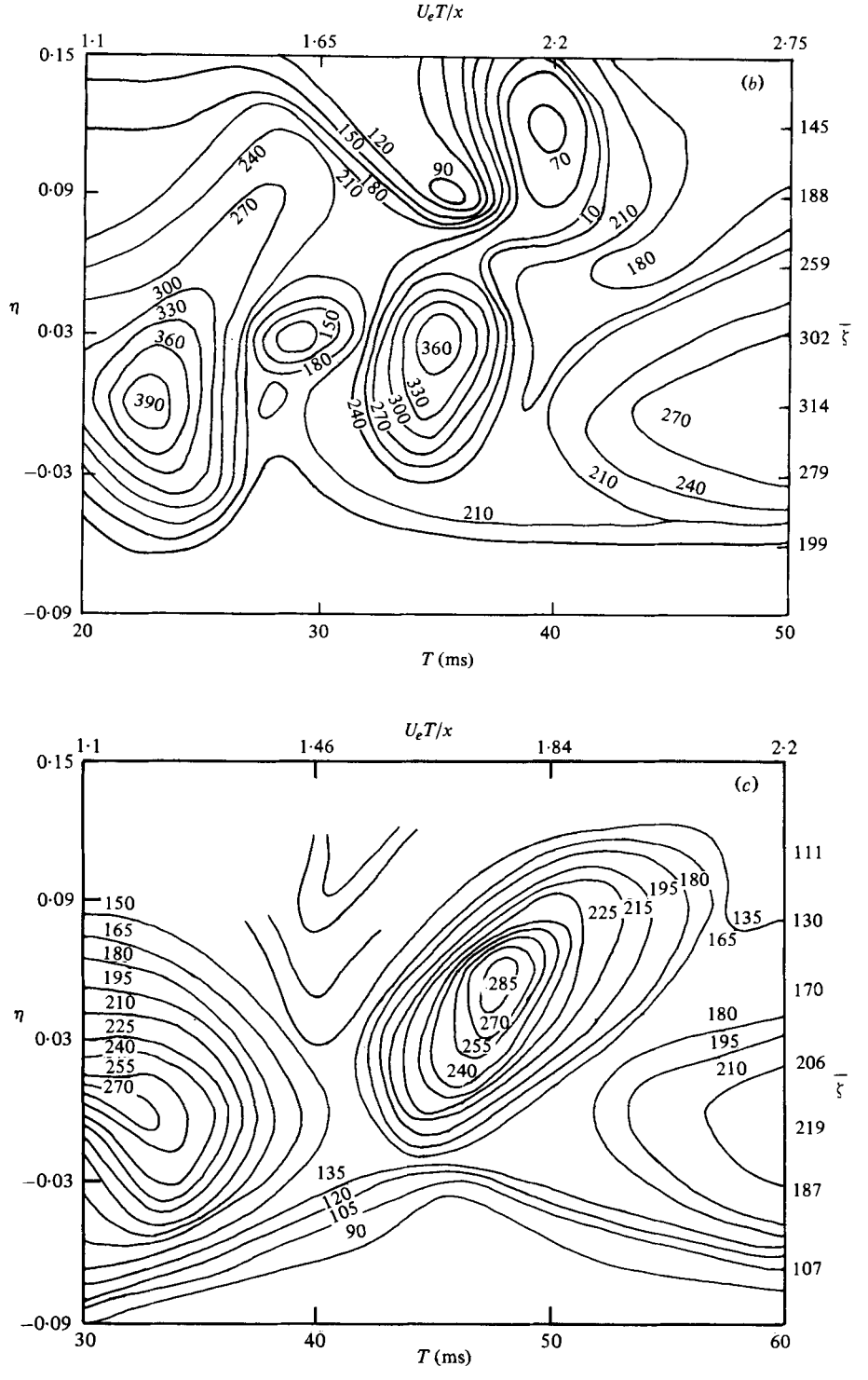

FIGURE 8. Contours of phase-average vorticity ζ_p (in s^{-1}). (*a*) $x/d = 1{\cdot}5$; (*b*) $x/D = 3{\cdot}0$; (*c*) $x/D = 4{\cdot}5$. Time mean value ζ corresponding to each η is indicated on the right boundary.

two complications. One is the direct effect of the streamwise convection velocity of the reference frame, which affects u_p but not v_p. The second is that the locations of peaks in the $u_p v_p$ contours are not associated with the vortex centres. Owing to the planetary motion of the peak-vorticity fluid around the spot centre (see later), vorticity contours are not helpful in providing accurate U_c data. The value of U_c was determined from $\langle\psi\rangle$ contours through an iterative process. That is, based on the u_p contours (see I), an initial guess of $U_c = 0{\cdot}7U_e$ was assumed. This value of U_c was used to compute $\langle\psi\rangle$ contours at the three stations (see later). From the locations of the centroids of these contours the value of U_c was found to be $0{\cdot}68U_e$, which was taken to be final value of U_c used in (4.2).

The applicability of the Taylor hypothesis to the deduction of spatial variations of large-scale coherent structure properties in the mixing layer is clearly questionable, as should be apparent from the governing equations. In addition to the explicit assumptions (i.e. negligible pressure gradient and viscous effects), the hypothesis involves the implicit assumptions regarding fluctuation intensity and shear rate (Lin 1953). On an instantaneous or phase-average basis, neither the shear rate nor the fluctuation level associated with the coherent structure is small. The remedy for this problem would be to repeat the phase-average measurements at different spatial locations of the structure cross-section, all at the same phase (Hussain & Zaman 1979). In the context of the present investigation, this approach was considered forbiddingly time-consuming and was not pursued.

An alternative but physically comprehensible way of interpreting (4.2) is to consider the velocity field $\mathbf{u}(\mathbf{x}, t)$ in the stationary reference frame and $\mathbf{u}^*(\mathbf{x}^*, t)$ in the reference frame convected downstream with a velocity U_c, i.e.

$$x_i^* = x_i - U_c t\delta_{1i}; \quad u_i^*(\mathbf{x}^*, t) = u_i(\mathbf{x}, t) - U_c\delta_{1i}, \tag{4.3}$$

where subscript 1 in the Kronecker delta δ_{ij} refers to the streamwise direction. Thus,

$$\left.\frac{\partial u_i(x,t)}{\partial t}\right|_x = \frac{\partial u_i^*}{\partial x_j^*}\frac{\partial x_j^*}{\partial t} + \frac{\partial u_i^*}{\partial t} = -U_c\frac{\partial u_i^*}{\partial x_1^*} + \frac{\partial u_i^*}{\partial t}. \tag{4.4}$$

Consequently, if an observer riding on the spot structure sees insignificant changes in the motion associated with the structure, $\partial u^*/\partial t$ can be neglected, and it is permissible to use the Taylor hypothesis (3.2). From this point of view, the situation is much more favourable in the boundary-layer spot where the streamwise rate of change of the structure is much slower and the spot has a self-preserving shape (Wygnanski *et al.* 1976) and where use of the Taylor hypothesis is justified even though considerations of shear rate and velocity fluctuation intensity would suggest otherwise. In the mixing layer, however, the spot structure undergoes far more rapid distortion compared to the rate of change of the scales; consequently, the use of the Taylor hypothesis is clearly questionable. The extent of the deviations introduced due to the use of the Taylor hypothesis in a mixing layer is being investigated in our laboratory.

The vorticity contours reveal interesting details of the flow dynamics. The spot-induced structure is marked by 'hills' and 'valleys' of the phase-average vorticity. Note that vorticity everywhere is of the same sign, as to be expected. On both left- and right-hand ends of figures 8 (*a*), (*b*) and (*c*), the two apparent large cells emphasize the spot in between. Since the spot structure is marked by significant coherent vorticity, the fluid outside the spot would randomly constitute either fine-grained turbulence of

the mixing layer, potential fluid or other naturally occurring structures. Measurements phase-locked onto the spot will accentuate the spot vorticity, as compared to the surounding vorticity. This is not to say that instantaneous vorticity in the turbulent fluid outside the spot is significantly lower, but that this random occurrence will smear out as well as lower the phase-average vorticity outside. Away from the spot, however, the phase-average vorticity should approach the time-mean vorticity of the mixing layer in the absence of the spot. Thus, on both left- and right-hand side ends, there should be half-cells approaching constant values (horizontal lines) forming two opposite U-turns at the boundaries. The tendency for the vorticity contours on the left boundary to close, indicating an apparent vorticity hill, is an artifact of the time shifts introduced in the realizations for optimum cross-correlation (see I). Owing to these time shifts, the vacated data locations (i.e. phases) are filled with zeroes; the consequence is the drop-off of vorticity at the left- and right-hand boundaries, resulting in an apparent closed-cell structure.

If the spot was embedded in the fine-scale turbulence or superimposed on the naturally occurring structure, the vorticity between the spot and the end cells would not drop significantly. The presence of low vorticity regions on either side of the spot suggests that low vorticity fluid elements, rather than naturally occurring structures, occupy the immediate vicinity of the spot. Consequently, it would appear that the spot is one of the naturally-occurring structures triggered by the spark.

The variation of the time-mean vorticity $\bar{\zeta}$ as a function of η in the mixing layer in the absence of the spot is indicated on the right-hand boundary. Note that the time-average vorticity progressively decreases with increasing x. The ratio of the peak spot vorticity to the time-mean vorticity at stations 1, 2, and 3 are 1·08, 1·15 and 1·30, respectively. This shows that the coherent-structure vorticity drops in x at a slower rate than the time-mean vorticity, as to be expected.

It is interesting to compare the vorticity contours at the three stations. At station 1, the positive vorticity cell is thin and extends across the entire width of the mixing layer, the peak being located at $T \approx 18$ ms and $\eta \approx -0{\cdot}03$ and moving forward with respect to the weaker outer part. Following the peaks and valleys of the vorticity contours from stations 1 to 2 and then from 2 to 3 suggests a clockwise rotation of the spot structure in the (η, T) plane. Note that the radially elongated coherent structure appears to shrink progressively, resulting in a single rounded structure at station 3. This does not necessarily represent a shrinking of the width of the vortical structure since the same $\Delta\eta$ values at station 3 represent three times the physical thickness of the layer at station 1. Thus, the vortical structure width does not seem to grow with x as fast as the flow width represented by the mean velocity profile. Due to lateral excursions of the structures (which increases with x), it is possible for the mean velocity profile to indicate a width of the mixing layer noticeably larger than the widths of inidividual structures.

At station 1, the region of minimum vorticity in front of the structure (figure 8*a*) is consistent with the low value of intermittency found there (see later) and is attributed to an apparent organization of the layer at the front of the structure. At this station, the noticeable difference between the spot centre identified by the pseudo-streamlines (or intermittency contours) and the vorticity contours indicates significant intensification of vorticity on the high-speed side leading edge (i.e. left-hand bottom corner of the spot).

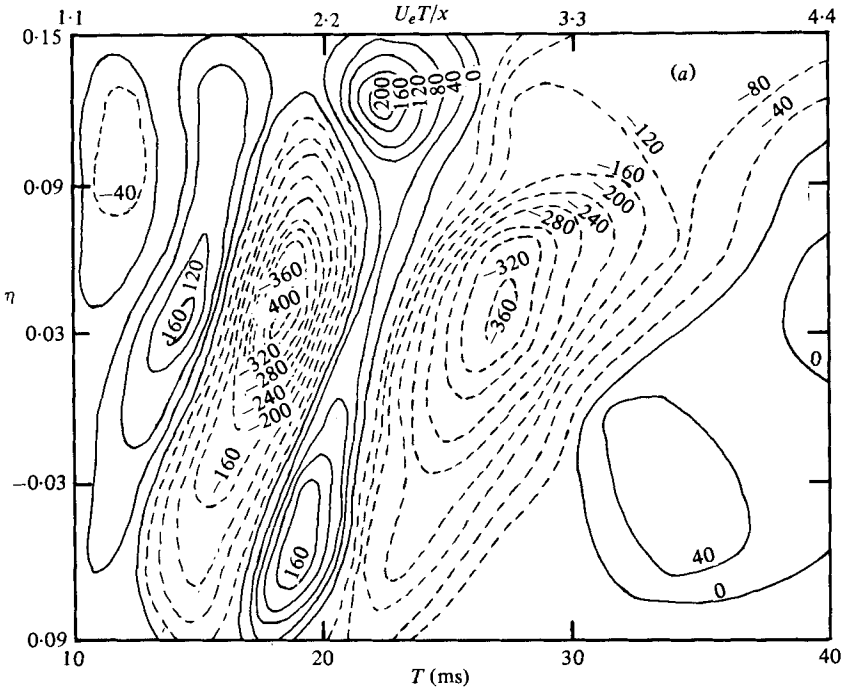

FIGURE 9 (*a*). For legend see page 121.

As with the $\tilde{u}_p\,\tilde{v}_p$ data, it may be interesting from a classical point of view, to examine the spot vorticity as a deviation from the time-mean vorticity (figures 9*a*, *b*, *c*). At station 1, the vorticity perturbation is essentially a deficit below the time-mean vorticity in the absence of the spot, except for a thin ridge of excess vorticity extending across the mixing-layer width. At a still lower T, there is another ridge of excess vorticity preceding the other ridge. Note that the excess vorticity peaks agree with the peaks of total vorticity contours at all the three stations. Following the vorticity contours from stations 1 to 3, it is clear that the peak phase-average vorticity perturbation moves progressively outward; these peaks also depict a clockwise rotation of the structure in the (η, T) plane.

4.4. *Phase-average streamlines*

The X-wire measurements provide phase-average time series of the orthogonal velocity components $u_p(r,t)$ and $v_p(r,t)$ of the spot structure at the probe location. Application of the Taylor hypothesis, using the structure-convection velocity U_c, would give the approximate spatial distribution of the spot velocity field $\mathbf{v} = (u_p, v_p)$ in the (x^*, r) plane, essentially at the phase when the spot is centred at the measurement station. The spot streamlines ψ_p in the (x^*, r) plane can be derived from the (u_p, v_p) data using the definition $\mathbf{v} \times \mathbf{ds} = 0$; thus, the slope of the phase-average streamline ψ_p at any location (x^*, r) is the ratio of v_p to u_p, i.e. $(dr/dx^*)_s = v_p/u_p$. Application of the method of isoclines can thus produce the streamlines at the phase corresponding to the (u_p, v_p) data.

However, in view of the fact that the mixing-layer spot is a complex entity which undergoes relatively rapid streamwise change, the success of the method will depend

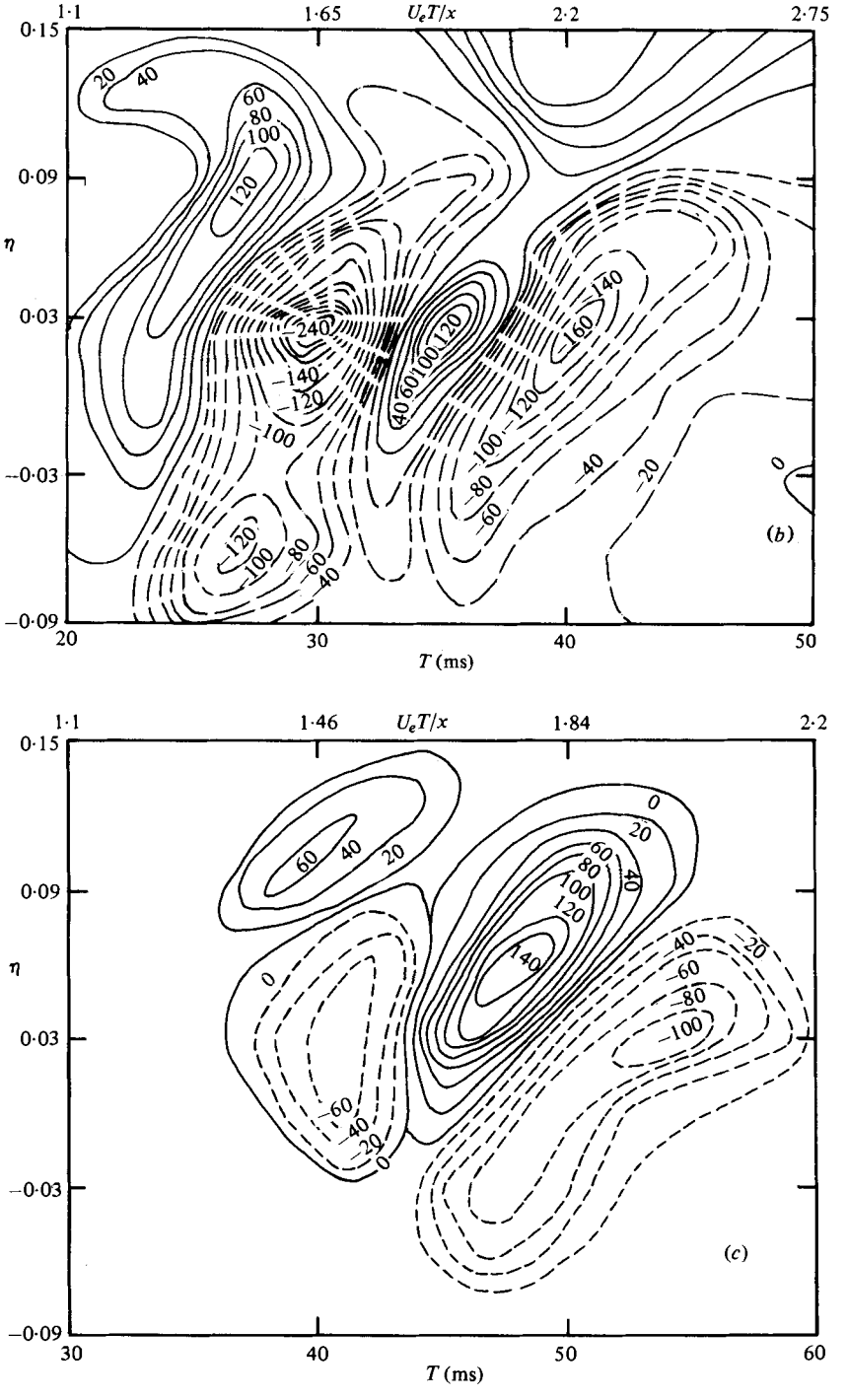

FIGURE 9. Contours of vorticity departure ζ_p (in s^{-1}). (*a*) $x/D = 1{\cdot}5$; (*b*) $x/D = 3{\cdot}0$; (*c*) $x/D = 4{\cdot}5$.

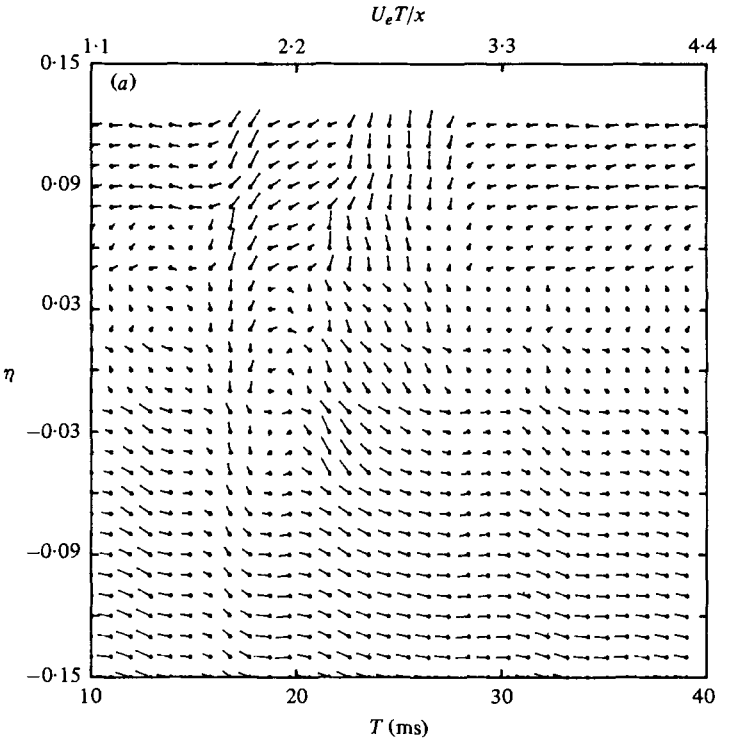

FIGURE 10 (*a*). For legend see page 124.

on the closeness at which data are available. The extremely time-consuming process of signal alignment through cross-correction (see I) before the phase-average velocity field (u_p, v_p) was derived, allowed us to take data at only a few (8) radial positions. Interpolation can be used to generate additional data at many intermediate radial positions. However, because of the large spatial variations in the velocity field associated with the spot [for example, see figure 3 (or figure 17 of I)], it was not considered worthwhile to generate the streamlines ψ_p through the distributions of the velocity slope v_p/u_p by applying the method of isoclines.

Figures 10(*a*), (*b*) and (*c*) show the distributions of the phase-average velocity vectors(u_p, v_p) in the (η,T) plane. The dots denote the origins of the vectors, the lines, their directions, and the lengths, the velocity magnitudes. These vector distributions are drawn with respect to a frame convected down stream with the structure velocity $U_c = 0{\cdot}68U_e$. Thus, the flow is towards decreasing T (i.e. increasing x) on the jet centreline and in the opposite direction on the outer edge. Note that, at the location of the spot, the velocity vectors do not indicate a simple flow pattern. The apparent complexity can be reduced by comparing the vector patterns with pseudo-stream-function contours (see later).

One can draw smooth lines connecting the vectors by following their directions. However, from practical considerations, hand-drawn contours connecting the vectors cannot be accurate since any bias can produce cumulative errors along a streamline without showing a clear conflict with the vector field. Figure 10(*d*) shows

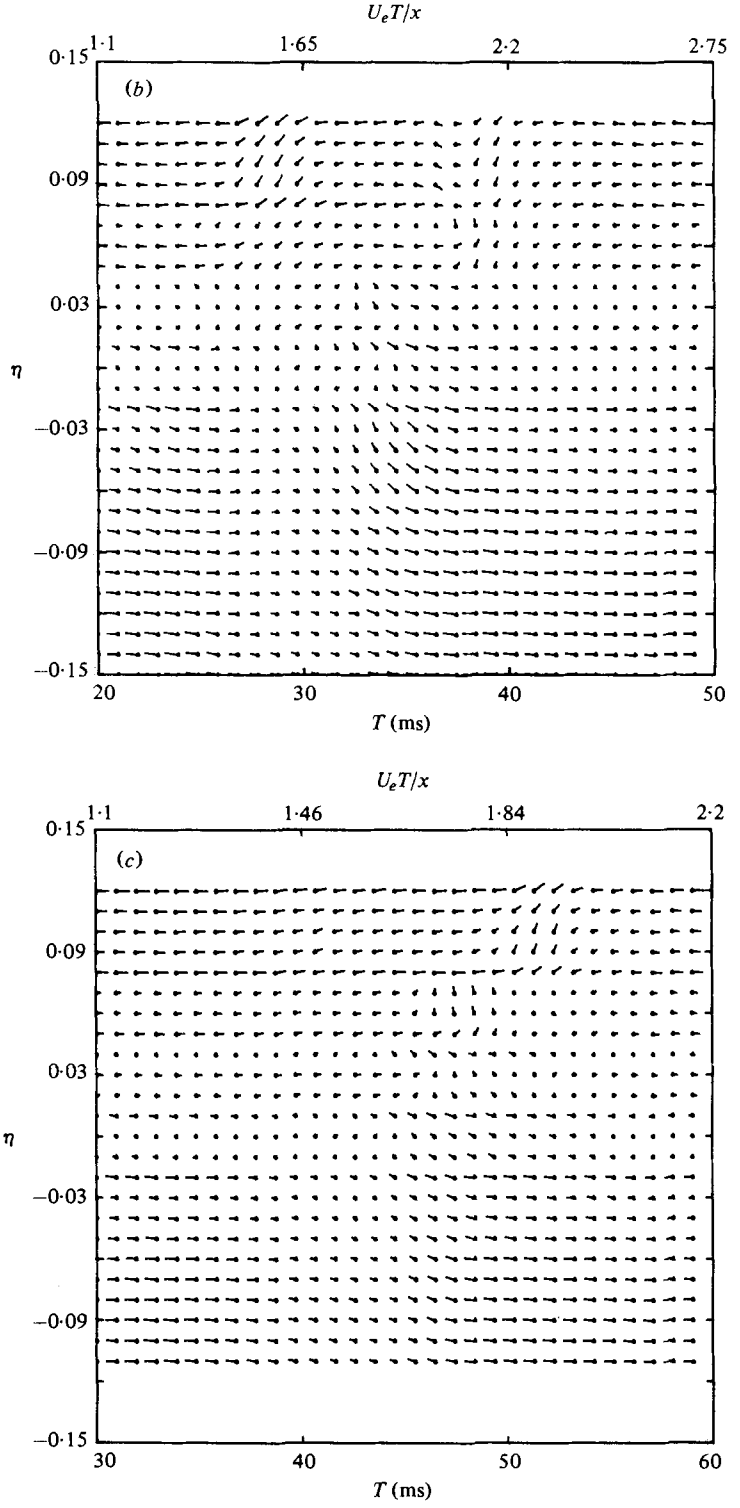

FIGURE 10 (*b*, *c*). For legend see page 124.

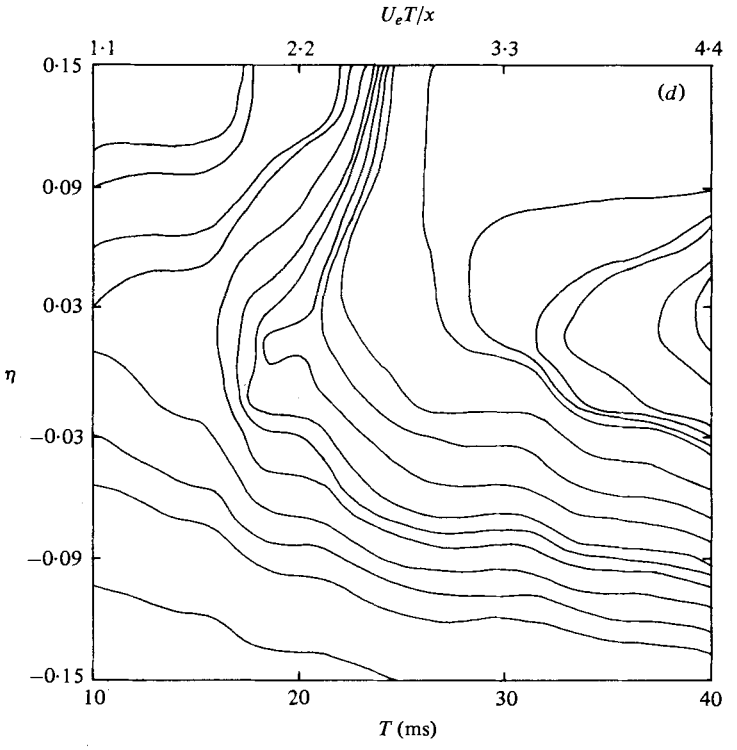

FIGURE 10. Phase average velocity vectors. (*a*) $x/D = 1{\cdot}5$; (*b*) $x/D = 3{\cdot}0$; (*c*) $x/D = 4{\cdot}5$; (*d*) streamlines corresponding to the vector field in (*a*).

one example of smooth streamlines corresponding to the vector fields shown in figure 10(*a*). While the streamline patterns depict the complicated velocity field in the spot, it is clear that the streamlines suggest a spot coherent structure different from what either u_p or v_p contours suggest separately (compare figure 10*d* with figure 3*a* in this part or figure 17*a* of I).

4.5. *Pseudo-stream-functions*

A phase-dependent stream function $\langle\psi(x,r)\rangle$ can be computed from the measured radial distributions $u_p(r)$ alone. Because these would be the true stream functions only under some restrictive assumptions outlined below (see also Hussain & Zaman 1979), these are called *pseudo-stream-functions* and the lines of their constant values, the *pseudo-streamlines*.

There is no reason for suspecting that the structure on the average is not symmetric with respect to the plane of symmetry (of the spark). It was inferred from the vorticity data that the spot is probably a naturally occurring one triggered by the spark. Furthermore, preliminary measurements at azimuthal angles 45°, 90°, 135°, 180° suggest that the spark-induced structure is nearly axisymmetric. This is also consistent with the low v_p magnitudes on the jet centre-line discussed earlier. Thus, one can assume the structure to be essentially axisymmetric. Under these assumptions, the incompressible flow continuity equation for the phase-average flow field is

$$\frac{\partial u_p}{\partial x}+\frac{1}{r}\frac{\partial}{\partial r}(rv_p)=0, \tag{4.5}$$

in terms of cylindrical co-ordinates (x, r, ϕ) with respect to the velocity components (u_p, v_p, w_p). Equation (4.5) assures that there exists a function $\langle\psi(x,r)\rangle$ such that $ru_p\,dr - rv_p\,dx$ is an exact differential $d\langle\psi\rangle$ of $\langle\psi\rangle$. That is,

$$u_p=\frac{1}{r}\frac{\partial\langle\psi\rangle}{\partial r}, \quad v_p=-\frac{1}{r}\frac{\partial\langle\psi\rangle}{\partial x}. \tag{4.6}$$

For the present case of the time-dependent coherent structure motion, the function $\langle\psi(x,r,t)\rangle$ is defined as

$$d\langle\psi\rangle = ru_p\,dr - rv_p\,dx+\frac{\partial\langle\psi\rangle}{\partial t}\,dt. \tag{4.7}$$

The consequence of $d\langle\psi\rangle$ being an exact differential is that its change between two points 1 and 2 (say (x_1, r_1, t_1) and (x_2, r_2, t_2)) is the difference between the values of $\langle\psi\rangle$ at the two points, i.e.

$$\langle\psi_2\rangle = \langle\psi_1\rangle+\int_1^2\left(ru_p\,dr - rv_p\,dx+\frac{\partial\langle\psi\rangle}{\partial t}\,dt\right). \tag{4.8}$$

If we now focus our attention at a fixed station (i.e x = constant) and at a particular time with respect to the spark trigger (i.e. t = constant), then

$$\langle\psi_1\rangle = \langle\psi_0\rangle+\int_0^r r^*u_p\,dr^*. \tag{4.9}$$

On the basis of the assumed axisymmetry, we can set $\langle\psi_0\rangle = 0$. Thus, from the radial variation of u_p alone, the phase-average distributions $\langle\psi\rangle$ can be determined at the phases corresponding to the u_p data.

Figures 11 (*a*), (*b*) and (*c*) show the pseudo-streamfunctions at the measurement stations, 1, 2, and 3, respectively, drawn with respect to a reference frame convected downstream with the velocity $U_c = 0{\cdot}68U_e$. That is, at any $t = t_1$,

$$\langle\psi(r,t_1)\rangle = \int_0^r r^*(u_p - U_c)\,dr^*. \tag{4.10}$$

Even though the integration in (4.10) would produce smooth contours of $\langle\psi\rangle$, comparison of the stream functions $\langle\psi\rangle$ with the streamlines ψ_p and vorticity contours is expected to reveal interesting aspects of the dynamics of the coherent structure.

In figures 11 (*a*)–(*c*), the transverse position η is indicated on the left-hand side; the $\langle\psi\rangle$ values are not shown for simplicity. Note that the spot-induced primary structure is located at $T \simeq 24{\cdot}2$ ms in station 1. The structure clearly extends beyond the time-average boundary of the layer on the low-speed side. The apparent secondary structure on the left (also in figure 10*b*, *c*) is merely a consequence of streamline reversal due to the reference frame convection velocity, since in the reference frame convected at $U_c = 0{\cdot}68U_e$ flow is towards decreasing time (i.e. increasing x) on the high-speed side and reverse on the low-speed side. The structure at $T \approx 33$ ms is an artifact resulting from numerical integration and presumably not the wake of the spot-induced structure; further downstream (i.e. in stations 2 and 3), this secondary structure disappears. Note that the integration method smooths out the detailed variations apparent in other contours.

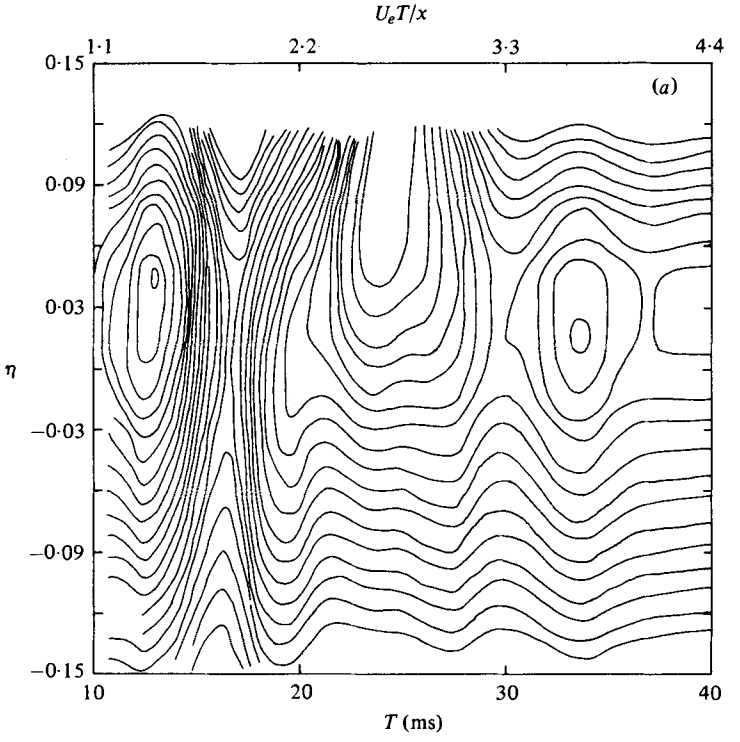

FIGURE 11 (*a*). For legend see page 127.

The streamline patterns based on the computed $\langle\psi\rangle$ contours, when compared with the velocity vector field data (figures 10*a*, *b*, *c*), permit a clearer interpretation of the vector field. Note that the vector field data in these figures would appear confusing but are quite consistent with the streamline patterns ψ_p. Figure 10(*a*) clearly shows that the spot is located nearer the outer edge of the layer at $T \simeq 24$ ms. Note that at stations 2 and 3, the structure has a blunt front but is tapered at its trailing edge. Note also that the front (downstream edge) occurs at an earlier time, i.e. to the left in figure 10(*a*). For discussion of comparisons between $\langle\psi\rangle$ contours and vorticity contours, see § 5.

4.6. *Intermittency contours*

From the classical, time-average view, the mixing layer is a region of turbulent flow increasing in width in the streamwise direction. However, high-speed flow visualization studies (for example, Clark 1979) show that the layer is often organized into vortical lumps of fluid connected by thin vortical regions called *braids*. Thus, the time-average intermittency profile at any station should be zero on either side of the mixing layer and maximum (but probably not 100%) in the middle of the mixing layer. Since the intermittency detection is based on an independent criterion and the γ_p contours are independent of reference frame convection, the γ_p contours should provide an essentially independent check on the spot boundaries deduced from the contours of u_p, v_p, u_pv_p, $\tilde{u}_p\tilde{v}_p$, ζ_p, $\tilde{\zeta}_p$, ψ_p and $\langle\psi\rangle$. Note that, unlike the contours of u_p, v_p, u_pv_p and ζ_p, the γ_p contours are simple and show reasonable agreement with the spot location

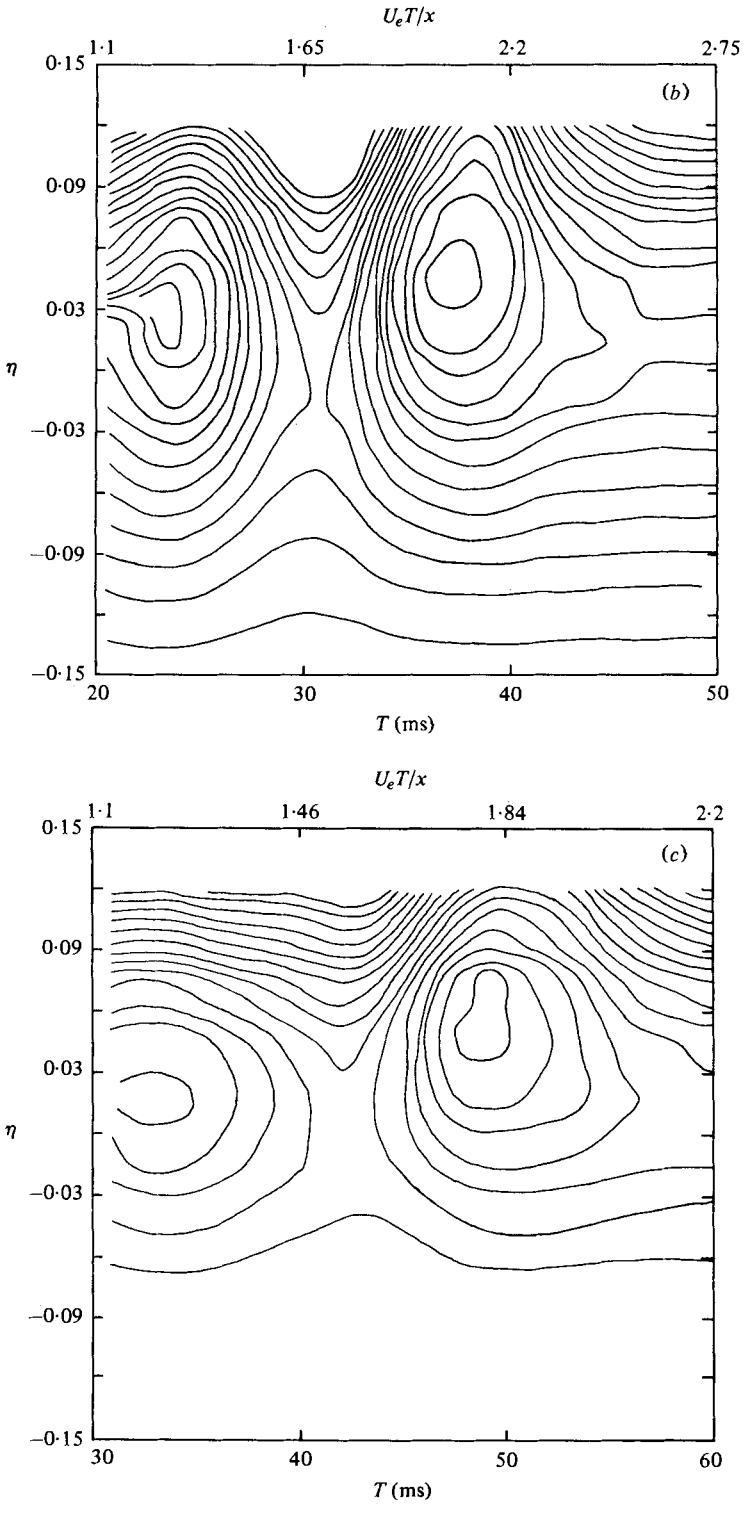

FIGURE 11. Contours of pseudo-stream-functions $\langle\psi\rangle$. (*a*) $x/D = 1{\cdot}5$; (*b*) $x/D = 3{\cdot}0$; (*c*) $x/D = 4{\cdot}5$.

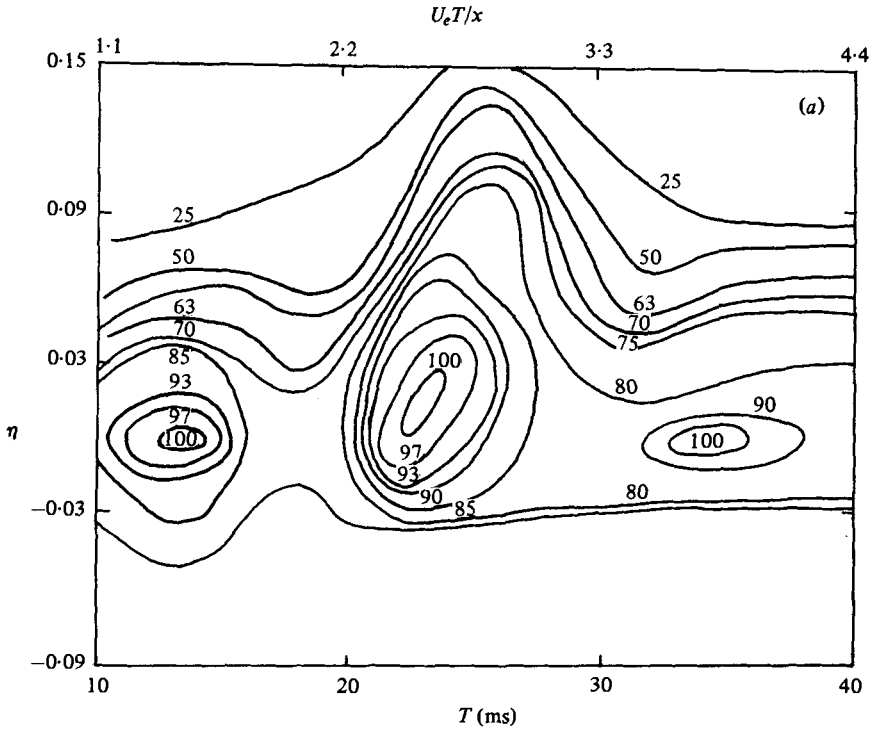

FIGURE 12 (*a*). For legend see page 129.

depicted by the ψ_p or $\langle\psi\rangle$ contours. Thus, in spite of the rough computation method involved, the pseudo-stream-function contours appear realistic.

The γ_p contours show that the spot extends outside the mixing layer on the low-speed side. Away from the spot, near the left- and right-hand side boundaries of the figures 12(*a*), (*b*) and (*c*), the intermittency distribution in η should match the time-average intermittency profile in the layer in the absence of the spot. The apparent presence of one structure in front (at a lower T) and at the rear (at a larger T) are artifacts due to the time shifts as discussed earlier. The low intermittency regions just in front and behind the spot, say at $T \approx 18$ ms and 30 ms in figure 12(*a*), are discussed below.

5. Dynamics of the spot

From the phase-average contours of $u_p, v_p, u_p v_p, \tilde{u}_p \tilde{v}_p, \zeta_p$ and $\hat{\zeta}_p$ which show a number of hills and valleys, it may appear that the spark-induced spot structure is an irregular entity, undergoing complex sets of distortions. This is definitely so in comparison to the boundary-layer spot, where the u_p contours alone show a self-preserving unicellular structure of a unique shape. However, if the phase-average pseudo-stream-function $\langle\psi\rangle$ or intermittency γ_p contours are considered, it is evident that the mixing-layer spot structure is comparatively simple, consisting of a large-scale, single entity. Note that sufficiently in front and behind the spot, the γ_p or $\langle\psi\rangle$ values should approach the corresponding mean values in the unperturbed mixing layer. Thus, because of the

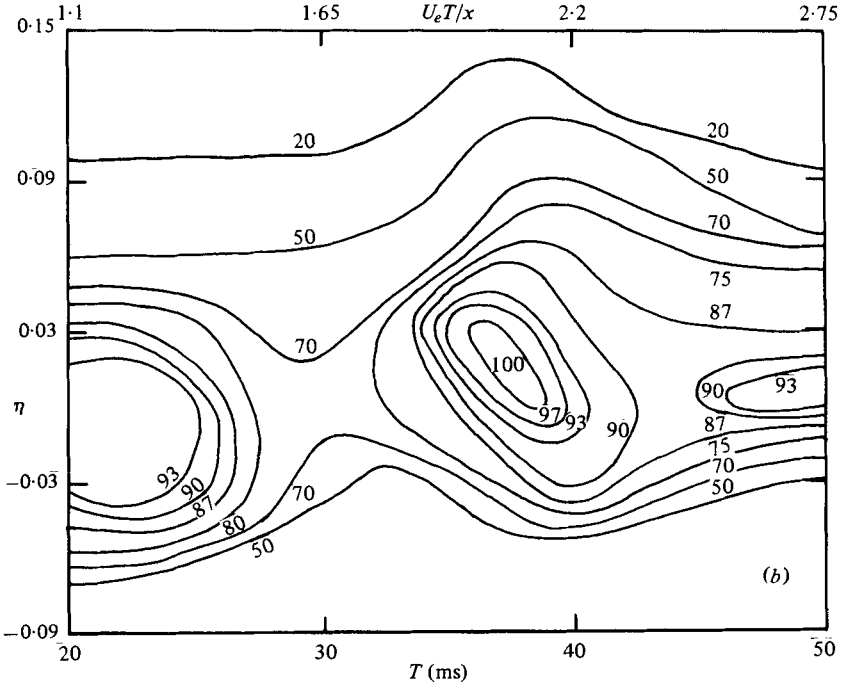

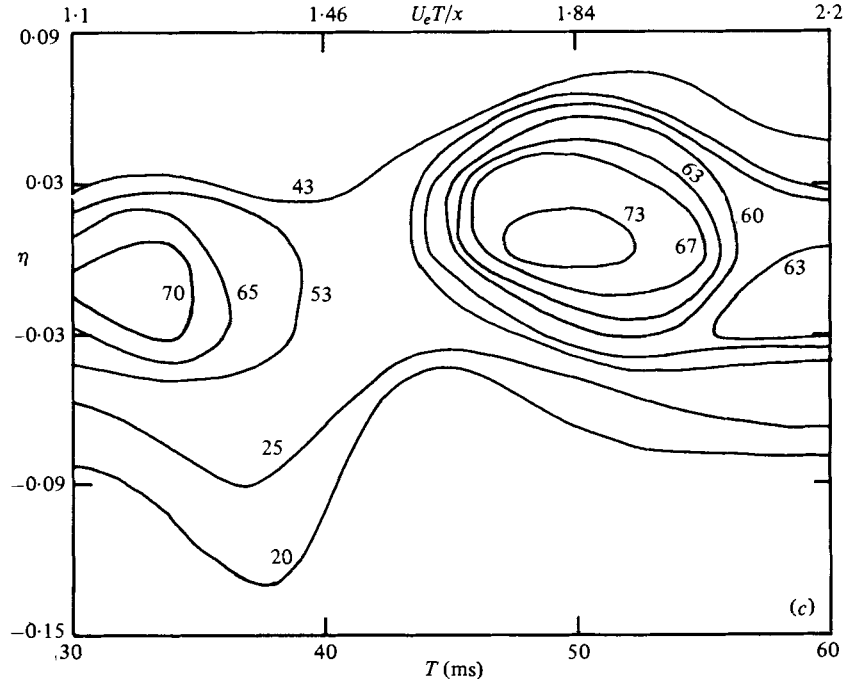

FIGURE 12. Contours of phase average intermittency γ_p. (*a*) $x/D = 1{\cdot}5$; (*b*) $x/D = 3{\cdot}0$; (*c*) $x/D = 4{\cdot}5$.

convection velocity U_c of the reference frame, the streamlines should form '$\supset$ and $\subset$ turns'. The apparent peaks formed on either end of the spot near the left- and right-hand boundaries of figures 11 and 12 are measurement artifacts at the ends of data time series discussed earlier.

The regions of low intermittency ahead and behind the spot in figures 12 (*a*), (*b*) and (*c*) need to be explained. If the spot was an energetic turbulent patch of fluid embedded in the middle of a fine-grained turbulent mixing layer, these low γ regions should not appear. The spot could be an independent entity superimposed on the naturally occurring mixing-layer structures or connected to the naturally occurring structures through braids. In either case, since the natural structures occur randomly in space and time, when their signatures are aligned with respect to each other, the spot structure will be highlighted and the intermittency will be high over its extent. The phase-average intermittency outside the spot due to the randomly occurring natural structures will be comparatively small. The orientations of the braids connecting the spot to the natural structures will also vary randomly, thus lowering intermittency outside the spot. Hence, the phase-average vorticity and intermittency outside the spot should be smaller.

Based on the above discussion, the spot boundaries deduced from γ_p and ζ_p data may be intuitively expected to be similar. Comparison of figures 8 and 12 reveal significant differences. One explanation is that even though γ_p is based on the vorticity, the γ_p and ζ_p are biased by different ranges of frequencies. The ζ_p data are based on smoothed derivatives of the low-pass filtered u_p and v_p data; thus, ζ_p contours are biased towards the low frequencies. On the other hand, γ_p, defined on the basis of the $|\partial v/\partial t| + A\,|\partial^2 v/\partial t^2|$ signal level, is biased towards the high frequencies. Even though higher vorticities are associated with smaller scales, ζ_p contours essentially identify large-scale motion associated with the spot. However, since the phase averaging in the determination of γ_p contours is taken after the $I(t)$ signal is obtained, the high-frequency information content in the γ_p contours is unaffected by the phase-average operation. These differences in their measurement techniques would permit differences between γ_p and ζ_p contours. Comparison of γ_p and ζ_p contours show that their centres do not agree either. If a γ_p contour is accepted as a boundary of the spot, the peak vorticity occurs on the front, high-speed end of the spot at station 1, just in front of it at station 2 and radially outside it in station 3 (see figure 12). This is consistent with the notion that the spark-induced structure undergoes large-scale rotation so that high vorticity fluid on the spot boundary undergoes planetary motion around the spot centre; the rotation is qualitatively depicted by the trajectory of the fluid marked by the vorticity peaks and valleys. Between stations 1 and 3 the rotation is seen to be about 160°. Note that the rotational trajectory of the vorticity peak-marked fluid around the spot centre is consistent with the pseudo-streamline patterns in figures 11 (*a*), (*b*) and (*c*) computed from u_p data, and that the v_p contours are also consistent with this explanation. The contours of constant pseudo-stream-functions, i.e. the pseudo-streamlines, are strongly dependent on the reference frame used. On the other hand, γ_p contours are invariant under Galilean transformation. In spite of these obvious differences, there is an amazing agreement on the spot boundaries as well as on the spot centres marked by γ_p and $\langle\psi\rangle$ contours. The spot centre marked by the $\langle\psi\rangle$ contours occurs at exactly the same T but at a larger η. This is attributed to the artifact of the convection velocity of the reference frame. For a given velocity profile, the η

location at which the relative velocity becomes zero progressively moves outwards with decreasing U_c.

The agreement between the spot centres indicated by the $\langle\psi\rangle$ and γ_p contours suggest that the computed stream functions are qualitatively correct. This agreement also justifies the derivation of the convection velocity U_c based on the $\langle\psi\rangle$ contours, as opposed to the ζ_p contours. However, because $\langle\psi\rangle$ is based on integration of u_p data only, the computed $\langle\psi\rangle$ contours are not expected to agree in detail with the streamline pattern deduced from the (u_p, v_p) distribution in the (x, y) plane; for example, compare figure 11 (*a*) with figure 10 (*a*), and especially with figure 10 (*d*). Because the streamwise convection velocity of the structure has been subtracted out, the detailed streamlines based on the vector (u_p, v_p) will be much more sensitive to the accuracy of the $v(t)$ measurement. Note that the leading edge of the spot has steep, closely-packed streamlines while the trailing edge is less steep. Both the $\langle\psi\rangle$ and γ_p contours show that sufficiently away from the spot, it has no influence on the basic flow and thus presumably on the naturally occurring structures. The low values of γ_p on the leading edge of the spot suggest stabilization of the flow field in front of the spot. The low intermittency and vorticity in front of the spot can be attributed to entrainment of the high-speed potential flow from the jet core in front of the spot. This suggestion is also consistent with the pseudo-streamline patterns (figure 11).

At station 1, the noticeable difference between the spot centre (identified) by the pseudo-streamlines or intermittency contours) and the vorticity contours indicates significant intensification of vorticity on the high-speed side leading edge (i.e. left-hand bottom corner of vorticity peak). Distributions of the phase average of the background-turbulence Reynolds stress $\langle u_r v_r\rangle$ show large negative values at this location. In order to relate the phase-average vorticity field to the turbulent field, it is necessary to derive the governing equation for the phase average vorticity $\langle\zeta_i\rangle$. Substituting the decomposition (2.1), i.e. $\zeta_i = \langle\zeta_i\rangle + \zeta_{ri}$, into the incompressible-flow vorticity equation, one gets

$$\frac{D}{Dt}[\langle\zeta_i\rangle + \zeta_{ri}] = [\langle\zeta_j\rangle + \zeta_{rj}]\frac{\partial}{\partial x_j}[\langle u_i\rangle + u_{ri}] + \nu\frac{\partial^2}{\partial x_k \partial x_k}[\langle\zeta_i\rangle + \zeta_{ri}]. \tag{5.1}$$

Note that the mean vorticity is included in the phase-average vorticity; this is an important point since, when the spot is present, the spot vorticity is the entire vorticity and not a peturbation over the time mean. Phase averaging the equation gives

$$\frac{\hat{D}}{Dt}\langle\zeta_i\rangle = \langle\zeta_j\rangle\frac{\partial\langle u_i\rangle}{\partial x_j} + \nu\nabla^2\langle\zeta_i\rangle - \frac{\partial}{\partial x_j}\langle u_{rj}\zeta_{ri}\rangle + \frac{\partial}{\partial x_j}\langle\zeta_{rj}u_{ri}\rangle. \tag{5.2}$$

If l is the characteristic size of the coherent spot structure and if ζ_{ri} and u_{ri} are well correlated, then

$$\frac{\partial}{\partial x_j}\langle u_{rj}\zeta_{ri}\rangle \approx \frac{\partial}{\partial x_j}\langle\zeta_{rj}u_{ri}\rangle \sim \frac{U_e^2}{\lambda l}, \quad \langle\zeta_j\rangle\frac{\partial\langle u_i\rangle}{\partial x_j} \sim \frac{U_e^2}{l^2}, \tag{5.3}$$

provided that $|u_{ri}| \sim |\langle u_i\rangle| = O(U_e)$ and $\langle\zeta_i\rangle \sim U_e|l$, $\zeta_{ri} = U_e/\lambda$. In the above, λ is the Taylor microscale defined such that $\langle(\partial u_i/\partial x_j)(\partial u_i/\partial x_j)\rangle = u^2/\lambda^2 = O(U_e^2/\lambda^2)$. Clearly, since $\lambda \ll l$, the coherent vortex stretching term on the right-hand side can be neglected. Independently, vortex stretching can be regarded as negligible in the axisymmetric flow. The stretching due to the changes in the toroid diameter is not likely to be large.

An estimate of the viscous term in (4.2) can also be obtained from

$$\nu\nabla^2\langle\zeta_i\rangle \Big/ \frac{\partial}{\partial x_j}\langle u_{rj}\zeta_{ri}\rangle \sim \frac{\nu U_e}{l^3}\Big/\frac{U_e^2}{\lambda l} = \frac{\nu\lambda}{l^2U_e} = \frac{\nu}{U_e l}\cdot\frac{\lambda}{l} = \frac{1}{R}\cdot\frac{\lambda}{l}. \tag{5.4}$$

Since the flow Reynolds number is very large and $l \gg \lambda$ the viscous diffusion is insignificant. This is also consistent with the notion that the turbulent flow dynamics is essentially inviscid. Since the structure transit time τ_T is of order l/U_e and the vorticity diffusion time τ_d is of order l^2/ν, the ratio of the two time scales $\tau_d/\tau_T = U_e l/\nu$ is very large, which also is another demonstration of the negligible effect of molecular diffusion on the coherent structure vorticity. Thus,

$$\frac{\hat{D}}{Dt}\langle\zeta_i\rangle \simeq \frac{\partial}{\partial x_j}\langle\zeta_{rj}u_{ri}\rangle - \frac{\partial}{\partial x_j}\langle u_{rj}\zeta_{ri}\rangle. \tag{5.5}$$

The left-hand side represents the material rate of change of the vorticity in the phase-average field and the right-hand side the generation of the phase-average vorticity through the velocity–vorticity fluctuations coherence terms indicated as body force terms (these can also be viewed as vortex forces, see Tennekes & Lumley 1972).

Further simplification of the equation can be introduced by specializing it for a flow homogeneous in the spanwise direction. That is, consider $\partial/\partial x_3$ of all phase-average quantities are zeroes. The equation then reduces to

$$\frac{\hat{D}}{Dt}\langle\zeta_3\rangle = +\frac{\partial}{\partial x_j}\langle\zeta_{rj}u_{r3}\rangle - \frac{\partial}{\partial x_j}\langle u_{rj}\zeta_{r3}\rangle, \tag{5.6a}$$

which, when dynamic pressure fluctuations are neglected, becomes

$$\frac{\hat{D}}{Dt}\zeta_p = -\frac{\partial^2}{\partial x^2}\langle u_r v_r\rangle + \frac{\partial^2}{\partial r^2}\langle u_r v_r\rangle, \tag{5.6b}$$

where ζ_p is the measured vorticity $\langle\zeta_3\rangle$. Note that the vorticity production will be largest in regions of *saddle points* in the $\langle u_r v_r\rangle$ contours. Following a streamline through the region of the leading edge of the structure on the high-speed side, i.e. through the location of vorticity peak ζ_p in figure 8(*a*), the differentiation of the $\langle u_r v_r\rangle$ data over the path gives a change consistent with the measured change in ζ_p indicated in figure 8(*a*). While the resolution of the data is not good enough to give a meaningful numerical value, one can note that the maximum changes of ζ_p occur at the 'saddle points' of the $\langle u_r v_r\rangle$ distributions.

Thus, the observed differences between the intermittency contours and the vorticity contours are the result of vorticity modification due to the spot-induced modulation of the background-turbulence Reynolds stress. Owing to the progressive weakening of the structure, these modulation effects become less pronounced and the vorticity contours become similar to the intermittency contours.

The maximum phase-average vorticity within the structures never deviates significantly from the time-average vorticity (figures 8*a–c*). Thus, the spark does not necessarily induce a strong artificial vortical structure, but serves to organize a naturally occurring rolled-up vortical structure. The phase-average vorticity away from the spot structure on the left-or right-hand ends is essentially that of the time-average vorticity.

Contour	$1 \rightarrow 2$	$2 \rightarrow 3$
$\langle\psi\rangle$	0·67	0·75
$u_p v_p$	0·72	0·72
γ_p	0·66	0·69

TABLE 1

The $u_p v_p$ contours show that the positive contours dominate the negative ones at each station. Thus, on the average, the spot transports momentum outward away from the jet centre-line. If the intermittency contours or the pseudo-streamline contours are compared with the $u_p v_p$ contours, it is clear that the structure region is directly responsible for the momentum transport. The $u_p v_p$ contour centres coincide with the corresponding γ_p or $\langle\psi\rangle$ contours. The positive transport of momentum outwards over the extent of the structure is due to the fact that the structure helps transport high-momentum fluid from the jet core outward.

Since the contour plots presented identify the time of detection of the structure centres at the three stations, these enable measurement of the structure convection velocity, depending on the contour chosen. The convection velocities in table 1 are measured for regions between stations 1 and 2 and between stations 2 and 3. The convection velocity of the spark-induced structure between stations 1 and 2 is slightly lower than that between stations 2 and 3. Considering the convection velocity profiles presented in I based on the characteristic features of the staggered $u_p(T)$ data, it is clear that the structure convection velocity is weighted by data mostly in the middle of the shear layer. Note that the convection velocities inferred from the three contours are within the experimental uncertainty.

6. Concluding remarks

In an attempt to investigate the dynamics of the large-scale coherent structure in the axisymmetric mixing layer, a coherent structure (called a 'spot' for simplicity) was induced by a spark triggered in the boundary layer preceding the lip of an axisymmetric mixing layer. The mixing-layer spot was educed by the method of iterative alignment of individual realizations through maximization of cross-correlation between individual realizations and ensemble average, and then the phase average over 200 realizations was obtained. Further signal enhancement was achieved through rejection of poorly aligned realizations.

The dynamics of the turbulent mixing-layer spot, whose signature is buried in the large-amplitude random fluctuations, is much more complicated than that of the boundary-layer spot. The eduction of the spot signature and interpretation of its flow physics is a formidable undertaking. Of all the phase-average contours, namely of u_p, v_p, $u_p v_p$, $\tilde{u}_p \tilde{v}_p$, ζ_p, $\tilde{\zeta}_p$, ψ_p, $\langle\psi\rangle$ and γ_p, the last two provide a better picture of the overall flow characteristics of the spot and are thus most reliable for identification of the spot convection velocity.

The spacing between sparks was so chosen that at a measurement station the passage time of a spot was less than 4 % of the interval between the spots. Thus there was no interaction between two induced spots. On either the front or the back of the

spot, the phase-average properties approach the constant time-mean values. Also, the 'zone averages' of u_r', v_r' and $\langle u_r v_r \rangle$ in the time interval containing the spot equal the values of these quantities in the same flow without the spot. These, together with the contour details, suggest that the spot is a naturally occurring structure triggered by the spark. The mechanism for the spot formation appears to be the generation of a pressure pulse by the spark and an associated nearly axisymmetric shear-layer roll-up. The relatively low v_p values on the jet centre-line also support this suggestion. The roll-up of the shear layer into an essentially axisymmetric vortical structure triggered by the spark suggests that the educed structure is not primarily the evolution of the boundary-layer spot that would be generated by the spark (Zilberman *et al.* 1977) simultaneously along with the shear layer roll-up. This boundary-layer spot may trail the structure but should decay because of lack of a sustaining mechanism. The apparent weak structure detected in the wake of the spot in the $\langle \psi \rangle$ contours at station 1 does not necessarily represent this decaying boundary-layer spot but is probably an artifact of numerical integration.

As the spark is fired, the shear layer is impulsively rolled up essentially into a toroidal vortical structure. This structure moves downstream transporting vortical fluid outwards, simultaneously entraining jet core fluid primarily at its front and ambient fluid primarily at its back. The Reynolds stress production associated with the spot is much larger than the background turbulence. The peak phase-average coherent Reynolds stress is found to be $0{\cdot}055U_e^2$ at all the three stations as compared to $0{\cdot}015U_e^2$ in the mixing layer without the spot.

By triggering the naturally occurring coherent structure with the help of a localized spark, we have been able to educe the large-scale coherent structure in an axisymmetric mixing layer. It has been possible to document the mixing-layer coherent structure in more detail than hitherto has been possible. It is not very likely that these details can be realistically captured for the naturally occurring structures in a mixing layer without involving cumbersome and tedious experimental approaches, primarily because of the inherent dispersion in shape, size, orientation and convection velocities of the natural structures as well as large radial variation in their organization (Lau & Fisher 1975; Bruun 1977; Yule 1978; Lau 1978, private communication; Hussain & Clark 1980). (Considering that the dynamics of the naturally occurring structures may indeed be different from the spot, measurements in undisturbed flows is clearly unavoidable and should be pursued.)

It is shown that the coherent structure plays a dominant role in entrainment and vorticity transport. Even though the Reynolds stress production by the coherent structure is significantly larger than that due to the background turbulence, the coherent-structure vorticity is not significantly larger than the mixing-layer mean vorticity. Since the Reynolds stress outside the spot is noticeably lower, it can be concluded that Reynolds stress production in the mixing layer is mostly due to the coherent structures.

The motivation of the present study was to characterize the large-scale coherent structure in the axisymmetric turbulent mixing layer. Presumably, an appropriate (random) superposition of these structures can lead to a physically sound model for turbulent shear flows. Even if it is granted that the spark-induced coherent structure reported here is a naturally occurring structure, it is clear that the structure is far from simple, and undergoes rapid and complex sets of motions through interactions

with naturally occurring structures. The complexity of the spot structure should challenge the theoretician to strive to develop a realistic turbulence model using the educed large-scale structure as a building block.

This research was supported by NSF Grant ENG 75-15226 and the Office of Naval Research Grant N00014–76–C–0128.

REFERENCES

BROWAND, F. K. & LAUFER, J. 1975 *Symp. on Turbulence in Liquids*, vol. 5, p. 333. Univ. of Missouri-Rolla.

BROWN, G. L. & ROSHKO, A. 1974 *J. Fluid Mech.* **64**, 775.

BRUUN, H. H. 1977 *J. Fluid Mech.* **64**, 775.

CHANDRSUDA, C., MEHTA, R. D., WEIR, A. D. & BRADSHAW, P. 1978 *J. Fluid Mech.* **85**, 639.

CLARK, A. R. 1979 Ph.D. dissertation, University of Houston.

DAVIES, P. O. A. L. & BAXTER, D. R. J. 1978 *Structure and Mechanisms of Turbulence I* (ed. H. Fiedler), Lecture notes in physics, vol. 75, p. 125. Springer.

HUSSAIN, A. K. M. F. 1977 *Cardiovascular Flow Dynamics and Measurements* (ed. N. H. C. Hwang & N. Norman), p. 541. University Park Press.

HUSSAIN, A. K. M. F. & CLARK, A. R. 1980 (Submitted to *J. Fluid Mech.*)

HUSSAIN, A. K. M. F. & REYNOLDS, W. C. 1970 *J. Fluid Mech.* **41**, 241.

HUSSAIN, A. K. M. F. & ZAMAN, K. B. M. Q. 1975 *Proc. 3rd Interagency Symp. Transp. Noise, Univ. of Utah*, p. 314.

HUSSAIN, A. K. M. F. & ZAMAN, K. B. M. Q. 1980 *J. Fluid Mech.* (to appear).

HUSSAIN, A. K. M. F. & ZEDAN, M. F. 1978*a* *Physics Fluids* **21**, 1100.

HUSSAIN, A. K. M. F. & ZEDAN, M. F. 1978*b* *Physics Fluids* **21**, 1475.

KLEIS, S. J. 1974 Ph.D. dissertation, Michigan State University.

LAU, J. C. & FISHER, M. J. 1975 *J. Fluid Mech.* **67**, 299.

LIN, C. C. 1953 *Quart. Appl. Math.* **10**, 295.

OSTER, D., DZIOMBA, B., FIEDLER, H. & WYGNANSKI, I. 1978 *Structure and Mechanisms of Turbulence I* (ed. H. Fiedler), Lecture notes in physics, vol. 75, p. 48. Springer.

PUI, N. K. & GARTSHORE, I. S. 1978 *J. Fluid Mech.* **91**, 111.

SOKOLOV, M., HUSSAIN, A. K. M. F., KLEIS, S. J. & HUSAIN, Z. D. 1980 *J. Fluid Mech.* **28**, 65.

TENNEKES, H. & LUMLEY, J. L. 1972 *A First Course in Turbulence*. MIT Press.

WYGNANSKI, I., SOKOLOV, M. & FRIEDMAN, D. 1976 *J. Fluid Mech.* **78**, 785.

WINANT, C. D. & BROWAND, F. K. 1974 *J. Fluid Mech.* **63**, 237.

YULE, A. J. 1978 *J. Fluid Mech.* **89**, 413.

ZAMAN, K. B. M. Q. 1978 Ph.D. dissertation, University of Houston.

ZILBERMAN, M., WYGNANSKI, I. & KAPLAN, R. E. 1977 *Phys. Fluids* **20**, S258.